Philosophical Magazine

ISSN: (Print) (Online) Journal homepage: https://www.tandfonline.com/loi/tphm20

Numerical calculation of interstitial dumbbell-mediated transport coefficients in dilute crystalline systems with non-truncated correlations

Soham Chattopadhyay & Dallas R. Trinkle

To cite this article: Soham Chattopadhyay & Dallas R. Trinkle (2022): Numerical calculation of interstitial dumbbell-mediated transport coefficients in dilute crystalline systems with non-truncated correlations, Philosophical Magazine, DOI: 10.1080/14786435.2022.2120646

To link to this article: https://doi.org/10.1080/14786435.2022.2120646

PHILOSOPHICAL MAGAZINE
https://doi.org/10.1080/14786435.2022.2120646

Numerical calculation of interstitial dumbbell-mediated transport coefficients in dilute crystalline systems with non-truncated correlations

Soham Chattopadhyay and Dallas R. Trinkle

Department of Materials Science and Engineering, University of Illinois at Urbana-Champaign, Urbana, IL, USA

ABSTRACT
Interstitial dumbbell-mediated diffusion can affect segregation and precipitation properties of solutes in alloys under irradiated conditions. Accurate computation of transport coefficients for dumbbell-mediated diffusion thus becomes essential for modelling solute segregation under irradiation. In this work, we extend the Green's function approach, a general numerical approach, to compute accurate transport coefficients for interstitial dumbbell-mediated mechanisms in the dilute limit for arbitrary crystalline systems with non-truncated correlations in atomic diffusion. We also present results of tracer correlation factors, solute drag ratios and partial diffusion coefficient ratios in iron and nickel-based alloys computed with our approach, compare our results with existing results in the literature, and discuss some aspects of correlated solute-dumbbell motion.

ARTICLE HISTORY
Received 15 February 2022
Accepted 26 August 2022

KEYWORDS
Diffusion; Green's function; interstitial dumbbells

1. Introduction

Alloys used in nuclear reactor components are subjected to extreme environments that progressively degrade their performance over time due to harmful microstructural changes that occur under irradiation. Such phenomena commonly include: void swelling, which leads to formation and growth of cavities inside the material that reduces its strength and can cause macroscopic dimension change of the components (see Section 4.02.8.2 in [1] for a review of void swelling in austenitic stainless steels); radiation-induced segregation [2], which leads to non-uniform concentration profiles of chemical species in the alloy; and radiation-induced precipitation [2] of intermetallic phases leading to the loss of strength, toughness and corrosion resistance. These issues occur ubiquitously in alloys for structural applications in nuclear reactors such as ferritic/ferritic-martensitic [2–5] and austenitic steels [6,7] and Zircaloys [8]. They are induced by high-energy particles such as alpha particles and neutrons

CONTACT Dallas R. Trinkle ✉ dtrinkle@illinois.edu Department of Materials Science and Engineering, University of Illinois at Urbana-Champaign, Urbana, IL 61801, USA

produced in nuclear reactors which cause cascades of atomic displacements in a target material upon collision, leading to excess defects in the material [9].

Depending on the flux of such incident high energy particles, a far greater-than-equilibrium amount of vacancy-interstitial pairs (called Frenkel pairs) may be produced. Many of these excess vacancies and interstitials recombine quickly and annihilate, but a significant amount can survive recombination, setting up defect chemical potential gradients (CPGs) in the material, which produce atomic transport processes resulting in the aforementioned micro-structural changes. While excess vacancies can either coalesce with each other to produce new voids or diffuse towards and enlarge existing cavities in the alloy, causing swelling, both excess interstitial defects and vacancies can facilitate atomic diffusion as they themselves diffuse towards sinks such as grain boundaries and dislocations, leading to a non-uniform redistribution of alloying elements in the matrix. Such redistribution phenomena can be collectively called the Inverse Kirkendall Effect [10,11]. This is because unlike the Kirkendall effect in a diffusion couple [12,13], in irradiated alloys, net atomic fluxes are set up under defect CPGs. This may result in the vicinity of the defect sinks becoming either depleted of or enriched with certain atomic species, depending on the coupling of atomic fluxes with that of defects. For example, in [14], atomic scale simulations of Fe-Cr alloys of various compositions show that below a threshold temperature (depending on Cr content), positive flux coupling of Cr with interstitial atoms is stronger than the negative flux coupling of Cr with vacancies. At higher temperatures, this trend is reversed. This causes Cr enrichment at the grain boundaries at lower temperatures via interstitial-mediated diffusion and Cr depletion at higher temperatures due to vacancy-mediated diffusion.

Since vacancy-mediated diffusion is prevalent in a wide range of materials for various applications, it has been studied extensively in the literature, both theoretically as well as experimentally. On the other hand, interstitial defect-mediated diffusion in irradiated alloys is often more complicated due to the geometrical nature of such defects, and theoretical models for their transport behaviour require deeper attention. To date, only approximate methods exist to compute their transport properties that involve the truncation of correlations in atomic motion.

First principles simulations have shown that interstitial defects in metals involving atoms knocked out of lattice sites often occur in the form of 'dumbbells' in their most stable form [15–17]. This defect occurs when an atom that is too big to fit in an interstitial site is forced into it, and as a result, pushes a neighbouring atom out of its lattice site. The two atoms centred about an unoccupied lattice site form a 'dumbbell'. There can be two different kinds of these dumbbells depending on the chemical species of the two atoms. Whenever the two atoms are of the same species, either self-interstitial atoms (SIAs) or solutes, they are called pure dumbbells, while if they differ, they are called mixed dumbbells. Due to the directional nature of dumbbells, they can execute more complicated types of atomic jumps compared to vacancies [18]. They also have lower migration barriers than vacancies [19,20] and are able to form in irradiated materials in concentrations significant enough to affect atomic transport properties.

Such transport properties can be characterised via the Onsager transport coefficients that govern diffusion fluxes of atoms under small CPGs according to the relation

$$\mathbf{J}^{\alpha} = -\sum_{\beta} L^{\alpha\beta} \nabla \mu^{\beta} \tag{1}$$

where α and β correspond to chemical species, $\mathbf{J}^{\alpha}$ is the flux of species α, $\nabla \mu^{\beta}$ is the CPG of species β and $L^{\alpha\beta}$ are the Onsager transport coefficients that determine the amount of flux coupling between various species. These transport coefficients can therefore be used to characterise segregation behaviour of solutes via defect-mediated diffusion [14,21]. The transport coefficients depend on mechanisms of atomic jumps, and several methods exist in the literature to compute them. Often the most conceptually straightforward methods are stochastic methods. Although not used to compute transport coefficients explicitly, an early stochastic model used to study correlation effects in both vacancy- [22,23] and dumbbell-mediated diffusion [24] is the 'Encounter Model', which is based on stochastically computing the mean squared displacement of a tracer atom and the mean number of jumps of the tracer atom due to a single defect. Modern stochastic methods to compute transport coefficients are mainly variants of Kinetic Monte Carlo (KMC), based on the generalised Einstein relations for transport coefficients [25,26]. KMC methods are popular for their ease of implementation for dilute and concentrated systems alike. In addition to computing transport coefficients, they also allow the ability to study the microscopic evolution of the system with time. This enables, for example, direct atomic-scale visualisation of atomic segregation phenomena in alloys under irradiation [14,27–30]. Advanced KMC-based methods, such as the kinetic activation-relaxation technique [31,32] can also explore the energy landscape 'on-the-fly', self-identifying new defect configurations and transitions during the simulation. For computing transport coefficients, however, KMC methods are limited by potentially large simulation times to simulate long atomic trajectories required to obtain converged values. In [14] for example, transport coefficients were calculated by computing mean squared displacements over 10^5 trajectories, each containing 10^5 sequential atomic jumps.

Semi-analytical models to compute the transport coefficients can help overcome this limitation, although such models have some inherent errors due to either truncated energetic interactions between species or truncated range of correlations in atomic jumps. Some of these models for BCC and FCC systems can be found in [33–36]. More recently, the self-consistent mean field (SCMF) method was formulated for both vacancy and dumbbell-mediated transport [37–40]. This is a semi-analytical method that assumes close-to-equilibrium kinetics, and is based on approximating perturbations to equilibrium atomic configuration (or state) probabilities under a CPG using a 'kinetic' cluster expansion. The finite range of this cluster expansion corresponds to truncating long-ranged correlations between atomic displacements that can lead to some errors in the computed transport coefficients, although with sufficient convergence studies, accurate results can be obtained [41]. The SCMF method has also been extended recently to compute contributions of defect clusters to transport coefficients in arbitrary crystalline lattices with long-ranged solute-defect interactions, thereby providing more physical insight into diffusion mechanisms [41].

One of the most recent theoretical development towards Onsager transport coefficient computation is the Green's function method [42] that also assumes close-to-equilibrium kinetics. The Green's function method – which uses the Dyson equation to solve for the full Green's function in the presence of a solute – has been shown to truncate no correlations, and is applicable to arbitrary crystalline systems with solute-vacancy energetic interactions to any desired separation distance. Provided that the solute-induced changes in rate are localised to a finite set of states, then the corrected Green function can be computed without truncating the correlations to a finite range. As shown in [42], this allows for transport coefficients to be computed efficiently, requiring only a few seconds on a single processor at a given temperature, and with high accuracy through controllable numerical integration errors in the first Brillouin zone that show a power-law decay. Since variations in computed transport coefficients can arise both out of model approximation errors as well as variations in first principles energy schemes [43], such ability to efficiently compute transport coefficients with non-truncated correlations can also help quantify the variations propagated from uncertainties in the energies themselves as discussed in [43].

In this work, we extend the Green's function method to compute transport coefficients for dumbbell-mediated diffusion in the dilute limit in arbitrary lattices with non-truncated correlation effects. We then discuss some widely used flux coupling ratios useful in predicting segregation behaviour of solutes under irradiation, such as the drag ratio and partial diffusion coefficient ratio, and their origins based on correlated solute-defect motion and also compare our results to accurate data available in the literature to validate our model.

2. Methodology

2.1. Master equation and onsager transport coefficients

We consider an infinitely large crystalline solid and say that every arrangement of atoms on the lattice sites constitutes a *state* of the system. Diffusion via atomic jumps can then be viewed as transitions of the system from one state to another. The aim is to then arrive at an expression for the Onsager transport coefficients for the various chemical species (including defects) in terms of the properties of these states.

To do this, the Green's function method in [42] starts with the 'Master Equation' for mass transport,

$$\frac{\partial p_n}{\partial t} = -\sum_{n'} W_{n\to n'}\, p_n + \sum_{n'} W_{n'\to n}\, p_{n'} \tag{2}$$

Here, p_n denotes the thermodynamic probability of a state n, and $W_{n\to n'}$ denotes the rate of transition of the system from state n to state n' per unit time. The Master Equation stems from the assumption that diffusion is a Markovian process, where the residence time of the system at each state is large compared to the time it takes for the system to transition from one state to another. This means that the transition to the next state depends only on the current state.

Considering Equation (2) for every state n, the resulting system of equations can be written as

$$\frac{\partial \mathbf{p}}{\partial t} = \mathbf{W}^T\, \mathbf{p} \tag{3}$$

where the vector $\mathbf{p}$ has the probabilities of all the states n as its components and the transition rate matrix, $\mathbf{W}$, is given by

$$W_{n,n'} = \begin{cases} W_{n\to n'} & \text{if } n \neq n' \\ -\sum\limits_{n''\neq n} W_{n\to n''} & \text{if } n = n' \end{cases} \tag{4}$$

We work with a grand canonical ensemble of atoms, in which each species α in state n with chemical potential μ_α have their total number fixed at N^α at all times during the diffusion process. The equilibrium probability distribution of the states is then given by

$$p_n^0 = \exp\left[\frac{1}{k_B T}\left(\Phi_0 + \sum_\alpha \mu_\alpha N^\alpha - H(n)\right)\right] \tag{5}$$

where k_B is the Boltzmann constant, T is the temperature, $H(n)$ is the total energy of the atoms in the system in state n and Φ_0 is the grand potential and corresponds to a normalisation factor for the state probabilities.

We also assume that the transition rates satisfy detailed balance, which is a sufficient, but not a necessary condition for steady state, and is written as

$$p_n^0\, W_{n\to n'} = p_{n'}^0\, W_{n'\to n} \tag{6}$$

With the above definitions, the Onsager transport coefficients are given by [42]

$$L^{\alpha\beta} = \frac{1}{V_0 k_B T}\left[\frac{1}{2}\sum_{n,n'} p_n^0 W_{n\to n'}\,\delta\mathbf{x}^{\alpha}(n\to n')\otimes\delta\mathbf{x}^{\beta}(n\to n') + \sum_{n,n'} p_n^0 \mathbf{v}_n^{\alpha}\otimes G_{n,n'}\mathbf{v}_{n'}^{\beta}\right] \tag{7}$$

Here V_0 is the volume of the system and $\delta\mathbf{x}^{\alpha}(n\to n')$ is the displacement of species α when the system transitions from state n to state n'.

The velocity vector $\mathbf{v}_n^{\alpha}$ of species α in state n is defined by:

$$\mathbf{v}_n^{\alpha} = \sum_{n'} W_{n\to n'}\,\delta\mathbf{x}^{\alpha}(n\to n') \tag{8}$$

The matrix $\mathbf{G}$ is called the Green's function. It is the pseudo-inverse of the transition rate matrix and analogously to the lattice Green's function [44,45] satisfies

$$\sum_{n'} W_{n,n'} G_{n',n''} = \delta_{n,n''} \tag{9}$$

where δ denotes the Kronecker delta.

The first term within the brackets in Equation (7) is the uncorrelated contribution to the transport coefficient. The second term, through the Green's function, takes into account all correlations between states, with $G_{n,n'}$ being related to the total probability that the system ends up in state n' having started at state n [26,46]. To compute the transport coefficients, we must therefore compute the Green's function.

2.2. States and transitions in dumbbell-mediated diffusion in dilute systems

2.2.1. Solute-dumbbell states

As the first step towards evaluating the Green's function, we need to know the possible states of the system and the transition rates between these states via atomic jumps. In the present work, we consider the dilute limit, limiting ourselves to the interactions between a single solute with a single dumbbell in a lattice of N unit cells, where $N\to\infty$. The solute and SIA site concentrations in our model (c_s and c_i respectively) is considered to be $\frac{1}{N}$.

Figure 1 shows a schematic representation of the various types of states that can exist in an arbitrary crystalline lattice, along with the possible types of transitions among them during dumbbell-mediated diffusion. We can see from the figure that all the possible states of the system can be classified into two categories:

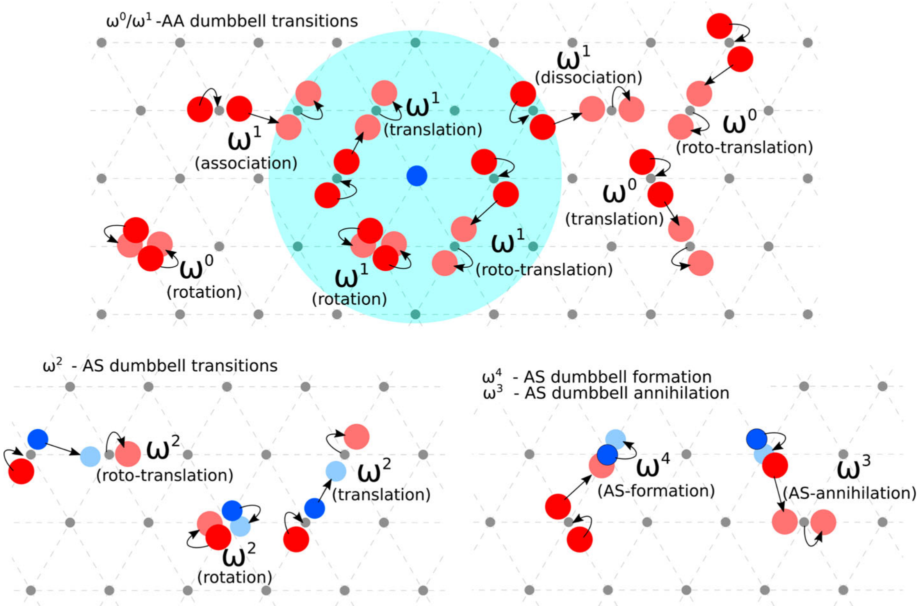

Figure 1. Mechanisms of dumbbell motion generally applicable to any crystalline system. The blue circles correspond to solute (S) atoms while the red circles correspond to solvent (A) interstitial atoms. The grey dots represent regular lattice sites occupied by A atoms. The classes of dumbbell motion considered are : ω^0 and ω^1 (top)– The ω^0 class consists of the motion of an AA dumbbell, outside the sphere of interaction with a solute (shown by the green circle around the solute), by either on-site rotation, translation or roto-translation. The ω^1 class of jumps consists of these same AA transitions within the solute's interaction range, along with association and dissociation with the solute by entering or leaving this interaction range, respectively; ω^2 (bottom-left)– Motion of an AS mixed dumbbell, which may include translation or roto-translation between sites, or on-site rotation; ω^4 and ω^3 (bottom-right) – The formation of an AS dumbbell from a solute and a neighboring AA dumbbell, and the annihilation of an AS dumbbell to form an associated solute-AA dumbbell pair, respectively. Although shown here with roto-translation mechanisms, these jumps can occur via other mechanisms as well such as rigid translations.

(1) Complex states – where a solute is at a substitutional site and a pure dumbbell is at any other site; we note that in our dilute limit analysis, pure dumbbells can only be formed by solvent SIAs. A complex state can be completely defined as $(\mathbf{R}_s\mathbf{u}_s\mathbf{R}_d\mathbf{u}_d\mathbf{o}_d)$. Here, $\mathbf{R}_s$ is the lattice vector to the unit cell containing the solute, while $\mathbf{R}_d$ is the lattice vector to the unit cell containing the pure dumbbell, with $\mathbf{R}_s$ as the reference. $\mathbf{u}_s$ $(\mathbf{u}_d)$ is a vector within the unit cell, pointing to the solute (dumbbell) location within the unit cell. The vector $\mathbf{o}_d$ joins the two interstitial atoms in the pure dumbbell and gives its orientation in space. We note that the complex state $\{\mathbf{R}_s\mathbf{u}_s\mathbf{R}_d\mathbf{u}_d\mathbf{o}_d\}$ is identical to $\{\mathbf{R}_s\mathbf{u}_s\mathbf{R}_d\mathbf{u}_d(-\mathbf{o}_d)\}$ since the two atoms forming the pure dumbbell are the same.

We define the formation energy of a complex state as

$$\Delta E_f(\mathbf{R}_s\mathbf{u}_s\mathbf{R}_d\mathbf{u}_d\mathbf{o}_d) = \Delta E_f(\mathbf{R}_s\mathbf{u}_s) + \Delta E_f(\mathbf{R}_d\mathbf{u}_d\mathbf{o}_d) + \delta E(\mathbf{R}_s\mathbf{u}_s\mathbf{R}_d\mathbf{u}_d\mathbf{o}_d) \quad (10)$$

where $\Delta E_f(\mathbf{R}_s\mathbf{u}_s)$ is the formation energy for a solute at $(\mathbf{R}_s + \mathbf{u}_s)$, $\Delta E_f(\mathbf{R}_d\mathbf{u}_d\mathbf{o}_d)$ is the formation energy for a pure dumbbell at $(\mathbf{R}_d + \mathbf{u}_d)$ with an orientation vector $\mathbf{o}_d$ without considering solute interaction, and is dependent in general on the orientation of the dumbbell. $\delta E(\mathbf{R}_s\mathbf{u}_s\mathbf{R}_d\mathbf{u}_d\mathbf{o}_d)$ is the binding energy between the solute and the pure dumbbell. Due to translational symmetry, we also note that all states related by a translation of the solute have the same energy, *i.e.*, $\Delta E_f(\mathbf{R}_s\mathbf{u}_s\mathbf{R}_d\mathbf{u}_d\mathbf{o}_d) = \Delta E_f(\mathbf{0}\mathbf{u}_s\mathbf{R}_d\mathbf{u}_d\mathbf{o}_d)$.

We then define as the *thermodynamic shell* the region around the solute, such that $\delta E(\mathbf{R}_s\mathbf{u}_s\mathbf{R}_d\mathbf{u}_d\mathbf{o}_d) \neq 0$. If a pure dumbbell is present outside of the thermodynamic shell, such that it has no energetic interactions with the solute, then we have $\delta E(\mathbf{R}_s\mathbf{u}_s\mathbf{R}_d\mathbf{u}_d\mathbf{o}_d) = 0$ and the formation energy of such a complex state is a simple sum of the formation energies of the solute and the pure dumbbell.

(2) Mixed states – these are the mixed dumbbells, where the solute atom is itself a part of the dumbbell, and which can move around by mixed dumbbell jump mechanisms as shown in Figure 1. Similar to complex states, a mixed state can be completely defined as $(\mathbf{R}_m\mathbf{u}_m\mathbf{o}_m)$, where $\mathbf{R}_m$ and $\mathbf{u}_m$ characterise the location of the site at which the mixed dumbbell is present and $\mathbf{o}_m$ is the orientation vector for the mixed dumbbell, which points to the interstitial solute atom by our convention. The mixed dumbbell formation energies $\Delta E_f(\mathbf{R}_m\mathbf{u}_m\mathbf{o}_m)$ may be computed in the same manner as pure dumbbell formation energies $\Delta E_f(\mathbf{R}_d\mathbf{u}_d\mathbf{o}_d)$. Also, due to translational symmetry $\Delta E_f(\mathbf{R}_m\mathbf{u}_m\mathbf{o}_m) = \Delta E_f(\mathbf{0}\mathbf{u}_m\mathbf{o}_m)$

2.2.2. Equilibrium state probabilities

Once we have identified the types of states, we can compute their equilibrium probabilities from their formation energies. We start by computing the partition function Z, the sum of the Boltzmann factors for all states, *i.e.*

$$Z = \sum_{\mathbf{R}_s\mathbf{u}_s\mathbf{R}_d\mathbf{u}_d\mathbf{o}_d} e^{-\Delta E_f(\mathbf{R}_s\mathbf{u}_s\mathbf{R}_d\mathbf{u}_d\mathbf{o}_d)/k_BT} + \sum_{\mathbf{R}_m\mathbf{u}_m\mathbf{o}_m} e^{-\Delta E_f(\mathbf{R}_m\mathbf{u}_m\mathbf{o}_m)/k_BT} \quad (11)$$

We can separate out the complex state contributions to Z into two further contributions – those from complex states where the pure dumbbell is within the thermodynamic shell around the solute at $(\mathbf{R}_s + \mathbf{u}_s)$, denoted as $\mathbf{R}_d\mathbf{u}_d\mathbf{o}_d \in TS(\mathbf{R}_s\mathbf{u}_s)$, and those when the pure dumbbells are outside the thermodynamic shell $(\mathbf{R}_d\mathbf{u}_d\mathbf{o}_d \notin TS(\mathbf{R}_s\mathbf{u}_s))$ with respect to the solute. From

Equation (10), for a complex state with $\mathbf{R}_\mathrm{d}\mathbf{u}_\mathrm{d}\mathbf{o}_\mathrm{d} \notin TS(\mathbf{R}_\mathrm{s}\mathbf{u}_\mathrm{s})$, the Boltzmann factor will be the product of the Boltzmann factors of the solute and the pure dumbbell forming at their respective sites without affecting each other. Their contribution to the partition function will be

$$\begin{aligned}
&\sum_{\mathbf{R}_\mathrm{s}\mathbf{u}_\mathrm{s}} \sum_{\mathbf{R}_\mathrm{d}\mathbf{u}_\mathrm{d}\mathbf{o}_\mathrm{d} \notin TS} e^{-\Delta E_f(\mathbf{R}_\mathrm{s}\mathbf{u}_\mathrm{s}\mathbf{R}_\mathrm{d}\mathbf{u}_\mathrm{d}\mathbf{o}_\mathrm{d})/k_BT} = \sum_{\mathbf{R}_\mathrm{s}\mathbf{u}_\mathrm{s}} e^{-\Delta E_f(\mathbf{R}_\mathrm{s}\mathbf{u}_\mathrm{s})/k_BT} \sum_{\mathbf{R}_\mathrm{d}\mathbf{u}_\mathrm{d}\mathbf{o}_\mathrm{d} \notin TS(\mathbf{R}_\mathrm{s}\mathbf{u}_\mathrm{s})} e^{-\Delta E_f(\mathbf{R}_\mathrm{d}\mathbf{u}_\mathrm{d}\mathbf{o}_\mathrm{d})/k_BT} \\
&\quad = N \sum_{\mathbf{u}_\mathrm{s}} e^{-\Delta E_f(\mathbf{0}\mathbf{u}_\mathrm{s})/k_BT} \left(\sum_{\mathbf{R}_\mathrm{d}\mathbf{u}_\mathrm{d}\mathbf{o}_\mathrm{d}} e^{-\Delta E_f(\mathbf{R}_\mathrm{d}\mathbf{u}_\mathrm{d}\mathbf{o}_\mathrm{d})/k_BT} - \sum_{\mathbf{R}_\mathrm{d}\mathbf{u}_\mathrm{d}\mathbf{o}_\mathrm{d} \in TS(\mathbf{0}\mathbf{u}_\mathrm{s})} e^{-\Delta E_f(\mathbf{R}_\mathrm{d}\mathbf{u}_\mathrm{d}\mathbf{o}_\mathrm{d})/k_BT} \right) \\
&\quad = N^2 \sum_{\mathbf{u}_\mathrm{s}} e^{-\Delta E_f(\mathbf{0}\mathbf{u}_\mathrm{s})/k_BT} \sum_{\mathbf{u}_\mathrm{d}\mathbf{o}_\mathrm{d}} e^{-\Delta E_f(\mathbf{0}\mathbf{u}_\mathrm{d}\mathbf{o}_\mathrm{d})/k_BT} \\
&\qquad - N \sum_{\mathbf{u}_\mathrm{s}} e^{-\Delta E_f(\mathbf{0}\mathbf{u}_\mathrm{s})/k_BT} \sum_{\mathbf{R}_\mathrm{d}\mathbf{u}_\mathrm{d}\mathbf{o}_\mathrm{d} \in TS(\mathbf{0}\mathbf{u}_\mathrm{s})} e^{-\Delta E_f(\mathbf{R}_\mathrm{d}\mathbf{u}_\mathrm{d}\mathbf{o}_\mathrm{d})/k_BT}
\end{aligned} \tag{12}$$

Since $N \to \infty$ and the thermodynamic shell encompasses a finite number of dumbbell states, we can retain only the leading order contribution in N so that

$$\begin{aligned}
\sum_{\mathbf{R}_\mathrm{s}\mathbf{u}_\mathrm{s}} \sum_{\mathbf{R}_\mathrm{d}\mathbf{u}_\mathrm{d}\mathbf{o}_\mathrm{d} \notin TS(\mathbf{R}_\mathrm{s}\mathbf{u}_\mathrm{s})} e^{-\Delta E_f(\mathbf{R}_\mathrm{s}\mathbf{u}_\mathrm{s}\mathbf{R}_\mathrm{d}\mathbf{u}_\mathrm{d}\mathbf{o}_\mathrm{d})/k_BT} &\approx N^2 \sum_{\mathbf{u}_\mathrm{s}} e^{-\Delta E_f(\mathbf{0}\mathbf{u}_\mathrm{s})/k_BT} \sum_{\mathbf{u}_\mathrm{d}\mathbf{o}_\mathrm{d}} e^{-\Delta E_f(\mathbf{0}\mathbf{u}_\mathrm{d}\mathbf{o}_\mathrm{d})/k_BT} \\
&= N^2 \overline{Z}
\end{aligned} \tag{13}$$

with $\overline{Z} = \sum_{\mathbf{u}_\mathrm{s}} e^{-\Delta E_f(\mathbf{0}\mathbf{u}_\mathrm{s})/k_BT} \sum_{\mathbf{u}_\mathrm{d}\mathbf{o}_\mathrm{d}} e^{-\Delta E_f(\mathbf{0}\mathbf{u}_\mathrm{d}\mathbf{o}_\mathrm{d})/k_BT}$. Note that we only need states within a single unit cell to compute $\overline{Z}$. The contributions from complex states with non-zero solute-dumbbell interaction will be $O(N)$ since

$$\begin{aligned}
&\sum_{\mathbf{R}_\mathrm{s}\mathbf{u}_\mathrm{s}} \sum_{\mathbf{R}_\mathrm{d}\mathbf{u}_\mathrm{d}\mathbf{o}_\mathrm{d} \in TS(\mathbf{R}_\mathrm{s}\mathbf{u}_\mathrm{s})} e^{-\Delta E_f(\mathbf{R}_\mathrm{s}\mathbf{u}_\mathrm{s}\mathbf{R}_\mathrm{d}\mathbf{u}_\mathrm{d}\mathbf{o}_\mathrm{d})/k_BT} = N \sum_{\mathbf{u}_\mathrm{s},\mathbf{R}_\mathrm{s}\mathbf{u}_\mathrm{d}\mathbf{o}_\mathrm{d} \in TS(\mathbf{0}\mathbf{u}_\mathrm{s})} e^{-\Delta E_f(\mathbf{0}\mathbf{u}_\mathrm{s}\mathbf{R}_\mathrm{d}\mathbf{u}_\mathrm{d}\mathbf{o}_\mathrm{d})/k_BT} \\
&\quad = N \sum_{\mathbf{u}_\mathrm{s}} e^{-\Delta E_f(\mathbf{0}\mathbf{u}_\mathrm{s})/k_BT} \sum_{\mathbf{R}_\mathrm{d}\mathbf{u}_\mathrm{d}\mathbf{o}_\mathrm{d}} e^{-\Delta E_f(\mathbf{0}\mathbf{u}_\mathrm{d}\mathbf{o}_\mathrm{d})/k_BT} e^{-\delta E(\mathbf{0}\mathbf{u}_\mathrm{s}\mathbf{R}_\mathrm{d}\mathbf{u}_\mathrm{d}\mathbf{o}_\mathrm{d})/k_BT}
\end{aligned} \tag{14}$$

and contributions from mixed dumbbell states will also be $O(N)$, since

$$\sum_{\mathbf{R}_\mathrm{m}\mathbf{u}_\mathrm{m}\mathbf{o}_\mathrm{m}} e^{-\Delta E_f(\mathbf{R}_\mathrm{m}\mathbf{u}_\mathrm{m}\mathbf{o}_\mathrm{m})/k_BT} = N \sum_{\mathbf{u}_\mathrm{m}\mathbf{R}_\mathrm{m}} e^{-\Delta E_f(\mathbf{0}\mathbf{u}_\mathrm{m}\mathbf{o}_\mathrm{m})/k_BT} \tag{15}$$

From Equations (13), (14) and (15), we can see that in the dilute limit, the contribution of the complex states with the dumbbells outside the thermodynamic shell will dominate, i.e.

$$Z \approx N^2 \overline{Z} \tag{16}$$

The equilibrium probability of a complex state then becomes

$$p^0_{\mathbf{R}_\mathrm{s}\mathbf{u}_\mathrm{s}\mathbf{R}_\mathrm{d}\mathbf{u}_\mathrm{d}\mathbf{o}_\mathrm{d}} = \frac{1}{N^2}\frac{e^{-\Delta E_f(\mathbf{R}_\mathrm{s}\mathbf{u}_\mathrm{s}\mathbf{R}_\mathrm{d}\mathbf{u}_\mathrm{d}\mathbf{o}_\mathrm{d})/k_BT}}{\overline{Z}} = c_s c_i \frac{e^{-\Delta E_f(\mathbf{0}\mathbf{u}_\mathrm{s}\mathbf{R}_\mathrm{d}\mathbf{u}_\mathrm{d}\mathbf{o}_\mathrm{d})/k_BT}}{\overline{Z}} \tag{17}$$

while that of a mixed dumbbell state becomes

$$p^0_{\mathbf{R}_\mathrm{m}\mathbf{u}_\mathrm{m}\mathbf{o}_\mathrm{m}} = \frac{1}{N^2}\frac{e^{-\Delta E_f(\mathbf{R}_\mathrm{m}\mathbf{u}_\mathrm{m}\mathbf{o}_\mathrm{m})/k_BT}}{\overline{Z}} = c_s c_i \frac{e^{-\Delta E_f(\mathbf{0}\mathbf{u}_\mathrm{m}\mathbf{o}_\mathrm{m})/k_BT}}{\overline{Z}} \tag{18}$$

where $c_s = c_i = \frac{1}{N}$ are our model's concentrations for the solute and the interstitial.

2.2.3. Transitions

The transitions among various pairs of states as schematically shown in Figure 1 can be classified as follows:

- ω^1 and ω^0 jumps – these jumps are of a pure dumbbell in a complex state, via rotation, translation, or roto-translation, with the solute remaining fixed in its position. This category also contains those transitions where the pure dumbbell associates or dissociates with the solute, i.e. it either comes within or leaves the thermodynamic shell. The rates for these jumps are denoted as $W^1_{\mathbf{R}_\mathrm{s}\mathbf{u}_\mathrm{s}\mathbf{R}_\mathrm{d}\mathbf{u}_\mathrm{d}\mathbf{o}_\mathrm{d}\to\mathbf{R}_\mathrm{s}\mathbf{u}_\mathrm{s}\mathbf{R}'_\mathrm{d}\mathbf{u}'_\mathrm{d}\mathbf{o}'_\mathrm{d}}$. Note that the solute site does not change in ω^1 jumps.

  We define $W^{0,d}_{\mathbf{R}_\mathrm{d}\mathbf{u}_\mathrm{d}\mathbf{o}_\mathrm{d}\to\mathbf{R}'_\mathrm{d}\mathbf{u}'_\mathrm{d}\mathbf{o}'_\mathrm{d}}$ to be the rate of a ω^1 jump when the dumbbell does not 'see' the solute, *i.e.*, the rate of the same dumbbell jump if the solute was absent and a regular solvent atom was present in its place. We then say that the rate of every ω^1 jump is the corresponding $W^{0,d}$ value, along with a correction term δW^1, that accounts for the interaction effects with the solute, i.e.

$$W^1_{\mathbf{R}_\mathrm{s}\mathbf{u}_\mathrm{s}\mathbf{R}_\mathrm{d}\mathbf{u}_\mathrm{d}\mathbf{o}_\mathrm{d}\to\mathbf{R}_\mathrm{s}\mathbf{u}_\mathrm{s}\mathbf{R}'_\mathrm{d}\mathbf{u}'_\mathrm{d}\mathbf{o}'_\mathrm{d}} = W^{0,d}_{\mathbf{R}_\mathrm{d}\mathbf{u}_\mathrm{d}\mathbf{o}_\mathrm{d}\to\mathbf{R}'_\mathrm{d}\mathbf{u}'_\mathrm{d}\mathbf{o}'_\mathrm{d}} + \delta W^1_{\mathbf{R}_\mathrm{s}\mathbf{u}_\mathrm{s}\mathbf{R}_\mathrm{d}\mathbf{u}_\mathrm{d}\mathbf{o}_\mathrm{d}\to\mathbf{R}_\mathrm{s}\mathbf{u}_\mathrm{s}\mathbf{R}'_\mathrm{d}\mathbf{u}'_\mathrm{d}\mathbf{o}'_\mathrm{d}} \tag{19}$$

  We note that when the pure dumbbell is outside the thermodynamic shell, the value of the correction term is zero, since the solute exerts no energetic influence on the dumbbell, so that $W^1_{\mathbf{R}_\mathrm{s}\mathbf{u}_\mathrm{s}\mathbf{R}_\mathrm{d}\mathbf{u}_\mathrm{d}\mathbf{o}_\mathrm{d}\to\mathbf{R}_\mathrm{s}\mathbf{u}_\mathrm{s}\mathbf{R}'_\mathrm{d}\mathbf{u}'_\mathrm{d}\mathbf{o}'_\mathrm{d}} = W^{0,d}_{\mathbf{R}_\mathrm{d}\mathbf{u}_\mathrm{d}\mathbf{o}_\mathrm{d}\to\mathbf{R}'_\mathrm{d}\mathbf{u}'_\mathrm{d}\mathbf{o}'_\mathrm{d}}$. Such pure dumbbell jumps where the solute is not considered to play a role in modifying the pure dumbbell jump rate are referred to as ω^0 jumps.

  The mechanisms of the ω^1 jumps place a few restrictions on their transition rates. We note that $\delta W^1_{\mathbf{R}_\mathrm{s}\mathbf{u}_\mathrm{s}\mathbf{R}_\mathrm{d}\mathbf{u}_\mathrm{d}\mathbf{o}_\mathrm{d}\to\mathbf{R}_\mathrm{s}\mathbf{u}_\mathrm{s}\mathbf{R}_\mathrm{s}\mathbf{u}_\mathrm{s}\mathbf{o}'_\mathrm{d}} = -W^{0,d}_{\mathbf{R}_\mathrm{d}\mathbf{u}_\mathrm{d}\mathbf{o}_\mathrm{d}\to\mathbf{R}_\mathrm{s}\mathbf{u}_\mathrm{s}\mathbf{o}'_\mathrm{d}}$, so that $W^1_{\mathbf{R}_\mathrm{s}\mathbf{u}_\mathrm{s}\mathbf{R}_\mathrm{d}\mathbf{u}_\mathrm{d}\mathbf{o}_\mathrm{d}\to\mathbf{R}_\mathrm{s}\mathbf{u}_\mathrm{s}\mathbf{R}_\mathrm{s}\mathbf{u}_\mathrm{s}\mathbf{o}'_\mathrm{d}} = 0$, since it is unphysical for a pure dumbbell to jump on to the same site as the solute and still remain a pure dumbbell. Similarly, $\delta W^1_{\mathbf{R}_\mathrm{s}\mathbf{u}_\mathrm{s}\mathbf{R}_\mathrm{s}\mathbf{u}_\mathrm{s}\mathbf{o}_\mathrm{d}\to\mathbf{R}_\mathrm{s}\mathbf{u}_\mathrm{s}\mathbf{R}'_\mathrm{d}\mathbf{u}'_\mathrm{d}\mathbf{o}'_\mathrm{d}} = -W^{0,d}_{\mathbf{R}_\mathrm{s}\mathbf{u}_\mathrm{s}\mathbf{o}_\mathrm{d}\to\mathbf{R}'_\mathrm{d}\mathbf{u}'_\mathrm{d}\mathbf{o}'_\mathrm{d}}$, since it is also unphysical for there to be an initial complex state where a pure dumbbell is at the same site as the solute. Also, as noted before, for any pair of complex states $(\mathbf{R}_\mathrm{s}\mathbf{u}_\mathrm{s}\mathbf{R}_\mathrm{d}\mathbf{u}_\mathrm{d}\mathbf{o}_\mathrm{d})$ and $(\mathbf{R}'_\mathrm{s}\mathbf{u}'_\mathrm{s}\mathbf{R}'_\mathrm{d}\mathbf{u}'_\mathrm{d}\mathbf{o}'_\mathrm{d})$ we have

$$W^1_{\mathbf{R}_\mathrm{s}\mathbf{u}_\mathrm{s}\mathbf{R}_\mathrm{d}\mathbf{u}_\mathrm{d}\mathbf{o}_\mathrm{d},\mathbf{R}'_\mathrm{s}\mathbf{u}'_\mathrm{s}\mathbf{R}'_\mathrm{d}\mathbf{u}'_\mathrm{d}\mathbf{o}'_\mathrm{d}} = \delta(\mathbf{R}_\mathrm{s} + \mathbf{u}_\mathrm{s} - \mathbf{R}'_\mathrm{s} - \mathbf{u}'_\mathrm{s})\, W^1_{\mathbf{R}_\mathrm{s}\mathbf{u}_\mathrm{s}\mathbf{R}_\mathrm{d}\mathbf{u}_\mathrm{d}\mathbf{o}_\mathrm{d},\mathbf{R}_\mathrm{s}\mathbf{u}_\mathrm{s}\mathbf{R}'_\mathrm{d}\mathbf{u}'_\mathrm{d}\mathbf{o}'_\mathrm{d}} \tag{20}$$

where

$$\delta(\mathbf{x}) = \begin{cases} 1 & \text{if } \mathbf{x} = \mathbf{0} \\ 0 & \text{otherwise} \end{cases} \tag{21}$$

Equation (20) says that unless the two complex states have the solute at the same location, the transition rate between one to the other is zero by definition.

We then define as the *kinetic shell* the region bounded by those sites around the solute, such that if a pure dumbbell were to form at one of these sites, then while it would have no energetic interaction with the solute ($\delta E = 0$), one or more types of ω^1 jumps from such a site would be an association jump (Figure 1), with $\delta W^1 \neq 0$. As we shall see in Section 2.4, even for systems without inversion symmetry, we only need complex states within the kinetic shell to compute the transport coefficients.

- ω^2 jumps – these are the jumps of a mixed dumbbell through which the solute can move as an interstitial defect via mixed dumbbell rotation, translation and roto-translation mechanisms as shown in Figure 1. The rates for these transitions are denoted as $W^2_{\mathbf{R}_\mathrm{m}\mathbf{u}_\mathrm{m}\mathbf{o}_\mathrm{m}\rightarrow\mathbf{R}'_\mathrm{m}\mathbf{u}'_\mathrm{m}\mathbf{o}'_\mathrm{m}}$.
- ω^3 and ω^4 jumps – ω^3 jumps correspond to the annihilation of a mixed dumbbell into a complex state. The solute returns as a substitutional defect to the site about which the mixed dumbbell was present, and the solvent interstitial atom forms a pure dumbbell at another site. The jump rates for this type of jump are denoted as $W^3_{\mathbf{R}_\mathrm{m}\mathbf{u}_\mathrm{m}\mathbf{o}_\mathrm{m}\rightarrow\mathbf{R}_\mathrm{m}\mathbf{u}_\mathrm{m}\mathbf{R}_\mathrm{d}\mathbf{u}_\mathrm{d}\mathbf{o}_\mathrm{d}}$. The reverse of the ω^3 jumps are called the ω^4 jumps and correspond to the formation of a mixed state from a complex state. One of the interstitial solvent atoms from a pure dumbbell jumps to the substitutional solute's site to form a mixed dumbbell. The rates for these jumps are denoted as $W^4_{\mathbf{R}_\mathrm{s}\mathbf{u}_\mathrm{s}\mathbf{R}_\mathrm{d}\mathbf{u}_\mathrm{d}\mathbf{o}_\mathrm{d}\rightarrow\mathbf{R}_\mathrm{s}\mathbf{u}_\mathrm{s}\mathbf{o}_\mathrm{m}}$. ω^3 and ω^4 jumps also have a similar restriction as Equation (20) due to the nature of their mechanisms, since not every mixed state can form from every complex state and vice versa. For any complex state $(\mathbf{R}_\mathrm{s}\mathbf{u}_\mathrm{s}\mathbf{R}_\mathrm{d}\mathbf{u}_\mathrm{d}\mathbf{o}_\mathrm{d})$ and mixed state $(\mathbf{R}_\mathrm{m}\mathbf{u}_\mathrm{m}\mathbf{o}_\mathrm{m})$ we have the following two conditions

$$W^4_{\mathbf{R}_\mathrm{s}\mathbf{u}_\mathrm{s}\mathbf{R}_\mathrm{d}\mathbf{u}_\mathrm{d}\mathbf{o}_\mathrm{d},\mathbf{R}_\mathrm{m}\mathbf{u}_\mathrm{m}\mathbf{o}_\mathrm{m}} = \delta(\mathbf{R}_\mathrm{s} - \mathbf{R}_\mathrm{m})\delta(\mathbf{u}_\mathrm{s} - \mathbf{u}_\mathrm{m})\, W^4_{\mathbf{R}_\mathrm{s}\mathbf{u}_\mathrm{s}\mathbf{R}_\mathrm{d}\mathbf{u}_\mathrm{d}\mathbf{o}_\mathrm{d},\mathbf{R}_\mathrm{s}\mathbf{u}_\mathrm{s}\mathbf{o}_\mathrm{m}} \tag{22}$$

$$W^3_{\mathbf{R}_\mathrm{m}\mathbf{u}_\mathrm{m}\mathbf{o}_\mathrm{m},\mathbf{R}_\mathrm{s}\mathbf{u}_\mathrm{s}\mathbf{R}_\mathrm{d}\mathbf{u}_\mathrm{d}\mathbf{o}_\mathrm{d}} = \delta(\mathbf{R}_\mathrm{s} - \mathbf{R}_\mathrm{m})\delta(\mathbf{u}_\mathrm{s} - \mathbf{u}_\mathrm{m})\, W^3_{\mathbf{R}_\mathrm{m}\mathbf{u}_\mathrm{m}\mathbf{o}_\mathrm{m},\mathbf{R}_\mathrm{m}\mathbf{u}_\mathrm{m}\mathbf{R}_\mathrm{d}\mathbf{u}_\mathrm{d}\mathbf{o}_\mathrm{d}} \tag{23}$$

We assume that ω^3 and ω^4 jumps always involve complex states within the kinetic shell, since they usually occur when the pure dumbbell and solute are nearest neighbours to each other, while the range of solute-dumbbell interactions can extend further.

From these definitions of our states and transitions amongst them, the Onsager transport coefficients can be written as:

$$\begin{aligned}
V_0 k_B T L^{\alpha\beta} = &\sum_{n\in\{\mathbf{R}_\mathrm{s}\mathbf{u}_\mathrm{s}\mathbf{R}_\mathrm{d}\mathbf{u}_\mathrm{d}\mathbf{o}_\mathrm{d}\}}\ \sum_{n'\in\{\mathbf{R}_\mathrm{s}\mathbf{u}_\mathrm{s}\mathbf{R}_\mathrm{d}\mathbf{u}_\mathrm{d}\mathbf{o}_\mathrm{d}\}} \\
& p_n^0\left[\frac{1}{2}W^1_{n\to n'}\,\delta\mathbf{x}^\alpha(n\to n')\otimes\delta\mathbf{x}^\beta(n\to n') + \mathbf{v}_n^\alpha\otimes G_{n,n'}\mathbf{v}_{n'}^\beta\right] \\
& + \sum_{n\in\{\mathbf{R}_\mathrm{m}\mathbf{u}_\mathrm{m}\mathbf{o}_\mathrm{m}\}}\ \sum_{n'\in\{\mathbf{R}_\mathrm{m}\mathbf{u}_\mathrm{m}\mathbf{o}_\mathrm{m}\}} \\
& p_n^0\left[\frac{1}{2}W^2_{n\to n'}\,\delta\mathbf{x}^\alpha(n\to n')\otimes\delta\mathbf{x}^\beta(n\to n') + \mathbf{v}_n^\alpha\otimes G_{n,n'}\mathbf{v}_{n'}^\beta\right] \\
& + \sum_{n\in\{\mathbf{R}_\mathrm{m}\mathbf{u}_\mathrm{m}\mathbf{o}_\mathrm{m}\}}\ \sum_{n'\in\{\mathbf{R}_\mathrm{s}\mathbf{u}_\mathrm{s}\mathbf{R}_\mathrm{d}\mathbf{u}_\mathrm{d}\mathbf{o}_\mathrm{d}\}} \\
& p_n^0\left[\frac{1}{2}W^3_{n\to n'}\,\delta\mathbf{x}^\alpha(n\to n')\otimes\delta\mathbf{x}^\beta(n\to n') + \mathbf{v}_n^\alpha\otimes G_{n,n'}\mathbf{v}_{n'}^\beta\right] \\
& + \sum_{n\in\{\mathbf{R}_\mathrm{s}\mathbf{u}_\mathrm{s}\mathbf{R}_\mathrm{d}\mathbf{u}_\mathrm{d}\mathbf{o}_\mathrm{d}\}}\ \sum_{n'\in\{\mathbf{R}_\mathrm{m}\mathbf{u}_\mathrm{m}\mathbf{o}_\mathrm{m}\}} \\
& p_n^0\left[\frac{1}{2}W^4_{n\to n'}\,\delta\mathbf{x}^\alpha(n\to n')\otimes\delta\mathbf{x}^\beta(n\to n') + \mathbf{v}_n^\alpha\otimes G_{n,n'}\mathbf{v}_{n'}^\beta\right]
\end{aligned} \tag{24}$$

where $\{\mathbf{R}_\mathrm{s}\mathbf{u}_\mathrm{s}\mathbf{R}_\mathrm{d}\mathbf{u}_\mathrm{d}\mathbf{o}_\mathrm{d}\}(\{\mathbf{R}_\mathrm{m}\mathbf{u}_\mathrm{m}\mathbf{o}_\mathrm{m}\})$ is the set of all possible complex (mixed) states that can form involving a single solute and interstitial dumbbell defect in an infinitely large solid.

2.3. The diffusion subspaces

We note that expression for the transport coefficient in Equation (24) is different from the case of vacancy-mediated diffusion, where, only one type of solute-defect configuration/state exists, the solute-vacancy complexes. A solute in a complex state can move when a vacancy is its neighbour. Hence, the last three terms in Equation (24) become irrelevant. In dumbbell-mediated diffusion, the solute is strictly immobile in complex states, whereas it is strictly mobile during ω^2 jumps. Thus, there are two distinct types of states and two resulting diffusion subspaces – the complex states where the solute *never* moves during atomic jumps, and the mixed dumbbell states where the solute *always* moves during atomic jumps, and the solute entering and leaving these two subspaces leads to its net diffusion. However, as we shall show in the following development, a formalism closely following that developed for the case of vacancy-mediated diffusion in [42] can be applied in dumbbell-mediated diffusion, with necessary changes to account for this additional diffusion space of mixed dumbbells.

From Figure 1, Equation (24) and the discussion in the previous paragraph, we can see that the complex and mixed dumbbell states divide the total transition rate matrix between states into a blocked structure of the form

$$\mathbf{W} = \begin{bmatrix} \mathbf{W}^1 & \mathbf{W}^4 \\ \mathbf{W}^3 & \mathbf{W}^2 \end{bmatrix} \tag{25}$$

The upper left diagonal block which consists of transitions only among complex states and constitutes the complex diffusion subspace, while the lower right diagonal block, which consists only of transitions among mixed states constitutes the mixed diffusion subspace. The off-diagonal blocks connect these two subspaces, through ω^4 (upper-right block) and ω^3 (lower-left block) jumps in $\mathbf{W}$. Note that for complex states, there can be $O(N)$ sites for the solute to occupy in the solid and $O(N)$ sites for the pure dumbbell, leading to $O(N^2)$ possible complex states. Accordingly, the block $\mathbf{W}^1$ is of size $O(N^2 \times N^2)$, although highly sparse due to each complex state being connected to only a few other complex states via atomic jumps. Since the mixed dumbbell can occupy $O(N)$ sites, leading to $O(N)$ mixed states, the block $\mathbf{W}^2$ is $O(N \times N)$.

The Green's function correspondingly has a blocked structure

$$\mathbf{G} = \begin{bmatrix} \mathbf{G}^1 & \mathbf{G}^4 \\ \mathbf{G}^3 & \mathbf{G}^2 \end{bmatrix} \tag{26}$$

where the upper left and lower right diagonal blocks contain correlations only within the complex and mixed diffusion subspaces respectively, and the off-diagonal blocks contain correlations between states in the two different diffusion subspaces. Unlike the transition rate matrix, the Green's function is in general a dense matrix, with the same dimensions as discussed above.

Clearly, explicit inversion of the transition rate matrix to compute the Green's function is an impossible task when $N \to \infty$. However, as shown in Appendix 1, due to translational symmetry we do not require individual elements of the Green's function matrix, but rather the sums of the elements over all final state unit cell locations of the solute. This can be used to re-write the correlated contribution to the transport coefficient $L_c^{\alpha\beta}$ in a reduced form as

$$\frac{V_0}{N} k_B T L_c^{\alpha\beta} = \left[(\mathbf{P^0 V})^{\alpha}_{\chi_0} | (\mathbf{P^0 V})^{\alpha}_{\phi_0} \right] \begin{bmatrix} \overline{\mathbf{G}^1} & \overline{\mathbf{G}^4} \\ \overline{\mathbf{G}^3} & \overline{\mathbf{G}^2} \end{bmatrix} \left[\mathbf{V}^{\beta}_{\chi_0} | \mathbf{V}^{\beta}_{\phi_0} \right]^T \tag{27}$$

The columns of the matrix block $\mathbf{V}^{\alpha}_{\chi_0}$ contain the velocity vectors of species α in those complex states where the solute is at $\mathbf{R}_s = \mathbf{0}$. Similarly, the columns of $\mathbf{V}^{\alpha}_{\phi_0}$ contain the velocity vectors of species α in mixed states with $\mathbf{R}_m = \mathbf{0}$. The matrix blocks $(\mathbf{P^0 V})^{\alpha}_{\chi_0}$ and $(\mathbf{P^0 V})^{\alpha}_{\phi_0}$ have the same columns, but each is also multiplied by the equilibrium probability of the corresponding state. The blocks of the reduced Green's function in Equation (27) now contain elements of the form

$$\begin{aligned}\overline{G^1}_{\mathbf{u}_\mathrm{s}\mathbf{R}_\mathrm{d}\mathbf{u}_\mathrm{d}\mathbf{o}_\mathrm{d},\mathbf{u}'_\mathrm{s}\mathbf{R}'_\mathrm{d}\mathbf{u}'_\mathrm{d}\mathbf{o}'_\mathrm{d}} &= \frac{1}{N}\sum_{\mathbf{R}_\mathrm{s},\mathbf{R}'_\mathrm{s}} G^1_{\mathbf{R}_\mathrm{s}\mathbf{u}_\mathrm{s}\mathbf{R}_\mathrm{d}\mathbf{u}_\mathrm{d}\mathbf{o}_\mathrm{d},\mathbf{R}'_\mathrm{s}\mathbf{u}'_\mathrm{s}\mathbf{R}'_\mathrm{d}\mathbf{u}'_\mathrm{d}\mathbf{o}'_\mathrm{d}} \\ &= \sum_{\mathbf{R}'_\mathrm{s}} G^1_{\mathbf{0}\mathbf{u}_\mathrm{s}\mathbf{R}_\mathrm{d}\mathbf{u}_\mathrm{d}\mathbf{o}_\mathrm{d},\mathbf{R}'_\mathrm{s}\mathbf{u}'_\mathrm{s}\mathbf{R}'_\mathrm{d}\mathbf{u}'_\mathrm{d}\mathbf{o}'_\mathrm{d}}\end{aligned} \tag{28a}$$

$$\overline{G^2}_{\mathbf{u}_\mathrm{m}\mathbf{o}_\mathrm{m},\mathbf{u}'_\mathrm{m}\mathbf{o}'_\mathrm{m}} = \frac{1}{N}\sum_{\mathbf{R}_\mathrm{m},\mathbf{R}'_\mathrm{m}} G^2_{\mathbf{R}_\mathrm{m}\mathbf{u}_\mathrm{m}\mathbf{o}_\mathrm{m},\mathbf{R}'_\mathrm{m}\mathbf{u}'_\mathrm{m}\mathbf{o}'_\mathrm{m}} = \sum_{\mathbf{R}'_\mathrm{m}} G^2_{\mathbf{0}\mathbf{u}_\mathrm{m}\mathbf{o}_\mathrm{m},\mathbf{R}'_\mathrm{m}\mathbf{u}'_\mathrm{m}\mathbf{o}'_\mathrm{m}} \tag{28b}$$

$$\overline{G^3}_{\mathbf{u}_\mathrm{m}\mathbf{o}_\mathrm{m},\mathbf{u}_\mathrm{s}\mathbf{R}_\mathrm{d}\mathbf{u}_\mathrm{d}\mathbf{o}_\mathrm{d}} = \frac{1}{N}\sum_{\mathbf{R}_\mathrm{m},\mathbf{R}_\mathrm{s}} G^3_{\mathbf{R}_\mathrm{m}\mathbf{u}_\mathrm{m}\mathbf{o}_\mathrm{m},\mathbf{R}_\mathrm{s}\mathbf{u}_\mathrm{s}\mathbf{R}_\mathrm{d}\mathbf{u}_\mathrm{d}\mathbf{o}_\mathrm{d}} = \sum_{\mathbf{R}_\mathrm{s}} G^3_{\mathbf{0}\mathbf{u}_\mathrm{m}\mathbf{o}_\mathrm{m},\mathbf{R}_\mathrm{s}\mathbf{u}_\mathrm{s}\mathbf{R}_\mathrm{d}\mathbf{u}_\mathrm{d}\mathbf{o}_\mathrm{d}} \tag{28c}$$

$$\overline{G^4}_{\mathbf{u}_\mathrm{s}\mathbf{R}_\mathrm{d}\mathbf{u}_\mathrm{d}\mathbf{o}_\mathrm{d},\mathbf{u}_\mathrm{m}\mathbf{o}_\mathrm{m}} = \frac{1}{N}\sum_{\mathbf{R}_\mathrm{s},\mathbf{R}_\mathrm{m}} G^4_{\mathbf{R}_\mathrm{s}\mathbf{u}_\mathrm{s}\mathbf{R}_\mathrm{d}\mathbf{u}_\mathrm{d}\mathbf{o}_\mathrm{d},\mathbf{R}_\mathrm{m}\mathbf{u}_\mathrm{m}\mathbf{o}_\mathrm{m}} = \sum_{\mathbf{R}_\mathrm{m}} G^4_{\mathbf{0}\mathbf{u}_\mathrm{s}\mathbf{R}_\mathrm{d}\mathbf{u}_\mathrm{d}\mathbf{o}_\mathrm{d},\mathbf{R}_\mathrm{m}\mathbf{u}_\mathrm{m}\mathbf{o}_\mathrm{m}} \tag{28d}$$

where the last equality in each of these equations follows from translational symmetry. As shown in Appendix 1, translational symmetry also provides that the reduced Green's function can be written as the inverse of a similarly reduced transition rate matrix

$$\begin{bmatrix} \overline{\mathbf{G^1}} & \overline{\mathbf{G^4}} \\ \overline{\mathbf{G^3}} & \overline{\mathbf{G^2}} \end{bmatrix} = \begin{bmatrix} \overline{\mathbf{W^1}} & \overline{\mathbf{W^4}} \\ \overline{\mathbf{W^3}} & \overline{\mathbf{W^2}} \end{bmatrix}^{-1} \tag{29}$$

Here, the blocks of the reduced transition rate matrix on the right hand side have the same form as the reduced Green's function in Equation (28). For clarity, we write out these elements below as well

$$\overline{W^1}_{\mathbf{u}_\mathrm{s}\mathbf{R}_\mathrm{d}\mathbf{u}_\mathrm{d}\mathbf{o}_\mathrm{d},\mathbf{u}'_\mathrm{s}\mathbf{R}'_\mathrm{d}\mathbf{u}'_\mathrm{d}\mathbf{o}'_\mathrm{d}} = \sum_{\mathbf{R}'_\mathrm{s}} W^1_{\mathbf{0}\mathbf{u}_\mathrm{s}\mathbf{R}_\mathrm{d}\mathbf{u}_\mathrm{d}\mathbf{o}_\mathrm{d},\mathbf{R}'_\mathrm{s}\mathbf{u}'_\mathrm{s}\mathbf{R}'_\mathrm{d}\mathbf{u}'_\mathrm{d}\mathbf{o}'_\mathrm{d}} \tag{30a}$$

$$\overline{W^2}_{\mathbf{u}_\mathrm{m}\mathbf{o}_\mathrm{m},\mathbf{u}'_\mathrm{m}\mathbf{o}'_\mathrm{m}} = \sum_{\mathbf{R}'_\mathrm{m}} W^2_{\mathbf{0}\mathbf{u}_\mathrm{m}\mathbf{o}_\mathrm{m},\mathbf{R}'_\mathrm{m}\mathbf{u}'_\mathrm{m}\mathbf{o}'_\mathrm{m}} \tag{30b}$$

$$\overline{W^3}_{\mathbf{u}_\mathrm{m}\mathbf{o}_\mathrm{m},\mathbf{u}_\mathrm{s}\mathbf{R}_\mathrm{d}\mathbf{u}_\mathrm{d}\mathbf{o}_\mathrm{d}} = \sum_{\mathbf{R}_\mathrm{s}} W^3_{\mathbf{0}\mathbf{u}_\mathrm{m}\mathbf{o}_\mathrm{m},\mathbf{R}_\mathrm{s}\mathbf{u}_\mathrm{s}\mathbf{R}_\mathrm{d}\mathbf{u}_\mathrm{d}\mathbf{o}_\mathrm{d}} \tag{30c}$$

$$\overline{W^4}_{\mathbf{u}_\mathrm{s}\mathbf{R}_\mathrm{d}\mathbf{u}_\mathrm{d}\mathbf{o}_\mathrm{d},\mathbf{u}_\mathrm{m}\mathbf{o}_\mathrm{m}} = \sum_{\mathbf{R}_\mathrm{m}} W^4_{\mathbf{0}\mathbf{u}_\mathrm{s}\mathbf{R}_\mathrm{d}\mathbf{u}_\mathrm{d}\mathbf{o}_\mathrm{d},\mathbf{R}_\mathrm{m}\mathbf{u}_\mathrm{m}\mathbf{o}_\mathrm{m}} \tag{30d}$$

We only need to compute the reduced Green's function for a finite number of states in the mixed dumbbell subspace since the indices $(\mathbf{u}_\mathrm{m}\mathbf{o}_\mathrm{m})$ and $(\mathbf{u}'_\mathrm{m}\mathbf{o}'_\mathrm{m})$ span the mixed dumbbell states allowed to occur in a single unit cell making the block $\overline{G^2}$ finite-dimensional. However, the dumbbell unit cell locations denoted by $\mathbf{R}_\mathrm{d}$ and $\mathbf{R}'_\mathrm{d}$ cover all unit cells in the infinitely large solid, making the block $\overline{G^1}$ of size $O(N \times N)$, and the blocks $\overline{G^3}$ and $\overline{G^4}$ of size $O(N)$ along the column and row dimension respectively. Thus, we see that even though translational symmetry reduces the dimensions of the matrix blocks by a factor of N, directly computing the matrix elements of Equation (28) is still not possible because of the infinitely large number of complex states that still need to be considered. In the next few sections, we first show that we don't need to consider all such complex states, and then discuss how to calculate the reduced Green's function elements corresponding to the complex states we do need.

2.4. Velocity vectors of complex states in arbitrary lattices

Beyond the kinetic shell, the velocity vectors of the solvent become identical to the case of just a pure dumbbell moving around without any solute in the solid due to no energetic interactions between the pure dumbbell and the solute, *i.e.*

$$\mathbf{v}^A_{\mathbf{0u}_\mathrm{s}\mathbf{R}_\mathrm{d}\mathbf{u}_\mathrm{d}\mathbf{o}_\mathrm{d}} = \mathbf{v}^A_{\mathbf{0u}_\mathrm{d}\mathbf{o}_\mathrm{d}} = \sum_{\mathbf{R}'_\mathrm{d}\mathbf{u}'_\mathrm{d}\mathbf{o}'_\mathrm{d}} W^{0,d}_{\mathbf{0u}_\mathrm{d}\mathbf{o}_\mathrm{d},\mathbf{R}'_\mathrm{d}\mathbf{u}'_\mathrm{d}\mathbf{o}'_\mathrm{d}} \delta\mathbf{x}^A(\mathbf{0u}_\mathrm{d}\mathbf{o}_\mathrm{d} \to \mathbf{R}'_\mathrm{d}\mathbf{u}'_\mathrm{d}\mathbf{o}'_\mathrm{d}) \tag{31}$$

for all complex states with the pure dumbbell outside the kinetic shell, where A denotes the solvent and $\mathbf{W}^{0,d}$ is the transition rate matrix for a pure dumbbell diffusing in a solid without any other defect in it. For systems with inversion symmetry, this velocity will be zero because any jump of the pure dumbbell will always have an equal and opposite symmetric counterpart. For such systems, we therefore only need to consider complex states with the pure dumbbell within the kinetic shell around the solute in Equation (27) to compute the correlated contribution to the transport coefficient.

For systems that do not have inversion symmetry, there may be non-zero velocity vectors for the solvent in complex states where the pure dumbbell is outside the kinetic shell. For such cases, we use the invariance principle of transport coefficients under modified displacements [46] to limit the state space to the same finite number of complex states as for systems with inversion symmetry. We first modify the solvent displacements during pure dumbbell jumps (with the solute remaining fixed) as

$$\begin{aligned}\widetilde{\delta\mathbf{x}}^A(\mathbf{0u}_\mathrm{s}\mathbf{R}_\mathrm{d}\mathbf{u}_\mathrm{d}\mathbf{o}_\mathrm{d} \to \mathbf{0u}_\mathrm{s}\mathbf{R}'_\mathrm{d}\mathbf{u}'_\mathrm{d}\mathbf{o}'_\mathrm{d}) = \delta\mathbf{x}^A(&\mathbf{R}_\mathrm{d}\mathbf{u}_\mathrm{d}\mathbf{o}_\mathrm{d} \\ &\to \mathbf{R}'_\mathrm{d}\mathbf{u}'_\mathrm{d}\mathbf{o}'_\mathrm{d}) + \mathbf{y}^A(\mathbf{0u}'_\mathrm{d}\mathbf{o}'_\mathrm{d}) - \mathbf{y}^A(\mathbf{0u}_\mathrm{d}\mathbf{o}_\mathrm{d})\end{aligned} \tag{32}$$

Where $\mathbf{y}^A(\mathbf{0u}_\mathrm{d}\mathbf{o}_\mathrm{d})$ is an arbitrary (bounded) vector assigned to complex states $\mathbf{0u}_\mathrm{s}\mathbf{R}_\mathrm{d}\mathbf{u}_\mathrm{d}\mathbf{o}_\mathrm{d}$ for all $\mathbf{u}_\mathrm{s}$ and $\mathbf{R}_\mathrm{d}$. If we then use these modified solvent displacements to compute the transport coefficients, the invariance principle dictates that they remain unchanged. We can utilise this by modifying the solvent displacements in a way that makes their velocity vectors zero for states where the pure dumbbell is outside the kinetic shell. Using Equation (32) to modify the displacements in Equation (31), we'll get modified velocities of the form

$$\widetilde{\mathbf{v}}^{A}_{\mathbf{0}\mathbf{u}_{\mathrm{s}}\mathbf{R}_{\mathrm{d}}\mathbf{u}_{\mathrm{d}}\mathbf{o}_{\mathrm{d}}} = \mathbf{v}^{A}_{\mathbf{0}\mathbf{u}_{\mathrm{d}}\mathbf{o}_{\mathrm{d}}} + \sum_{\mathbf{u}'_{\mathrm{d}}\mathbf{o}'_{\mathrm{d}}} \left(\sum_{\mathbf{R}'_{\mathrm{d}}} W^{0,d}(\mathbf{R}'_{\mathrm{d}}) \right)_{\mathbf{u}_{\mathrm{d}}\mathbf{o}_{\mathrm{d}},\mathbf{u}'_{\mathrm{d}}\mathbf{o}'_{\mathrm{d}}} \mathbf{y}^{A}(\mathbf{0}\mathbf{u}'_{\mathrm{d}}\mathbf{o}'_{\mathrm{d}}) \tag{33}$$

In order to then make these modified velocities zero, we can use

$$\mathbf{y}^{A}(\mathbf{0}\mathbf{u}_{\mathrm{s}}\mathbf{R}_{\mathrm{d}}\mathbf{u}_{\mathrm{d}}\mathbf{o}_{\mathrm{d}}) = \mathbf{y}^{A}(\mathbf{0}\mathbf{u}_{\mathrm{d}}\mathbf{o}_{\mathrm{d}}) = -\sum_{\mathbf{u}'_{\mathrm{d}},\mathbf{o}'_{\mathrm{d}}} \left(\sum_{\mathbf{R}'_{\mathrm{d}}} W^{0,d}(\mathbf{R}'_{\mathrm{d}}) \right)^{\dagger}_{\mathbf{u}_{\mathrm{d}}\mathbf{o}_{\mathrm{d}},\mathbf{u}'_{\mathrm{d}}\mathbf{o}'_{\mathrm{d}}} \mathbf{v}^{A}_{\mathbf{0}\mathbf{u}'_{\mathrm{d}}\mathbf{o}'_{\mathrm{d}}} \tag{34}$$

with † denoting pseudo-inverse. Using these vectors to modify the solvent displacements during pure dumbbell jumps, we can see from Equation (33) that its velocity vectors become zero in complex states where pure dumbbells are outside the kinetic shell. We therefore don't need to consider these states in equation Equation (27), just like systems with inversion symmetry. Note that this procedure needs to be repeated at every temperature due to changing transition rates.

2.5. Matrix symmetrization

As a prior step to computing the required Green's function elements in Equation (28), we first rewrite this equation in terms of symmetrised matrices since they are numerically more favourable. We first symmetrise the rate matrix in Equation (25) by defining

$$\Omega_{nn'} = (p^{0}_{n})^{\frac{1}{2}} W_{n,n'} (p^{0}_{n'})^{-\frac{1}{2}} \tag{35}$$

where the states n and n' can correspond to complex or mixed dumbbell states. Using detailed balance, it can be shown that $\Omega_{nn'} = \Omega_{n'n}$. The inverse of this matrix is then the symmetrised Green's function $\mathbf{g}$, with elements

$$g_{nn'} = (p^{0}_{n})^{\frac{1}{2}} G_{n,n'} (p^{0}_{n'})^{-\frac{1}{2}} \tag{36}$$

with $g_{nn'} = g_{n'n}$. Note that $\mathbf{\Omega}$ and $\mathbf{g}$ also have the same blocked structure as $\mathbf{W}$ and $\mathbf{G}$ as discussed before. We then define *bias vectors* for species α in state n as

$$\mathbf{b}^{\alpha}_{n} = (p^{0}_{n})^{\frac{1}{2}} \mathbf{v}^{\alpha}_{n} \tag{37}$$

where for complex states, we use the modified velocity vectors as discussed in the previous section.

Noting that the state probabilites are translationally invariant, the correlated contribution to the transport coefficient can then be written in terms of the bias vectors and $\mathbf{g}$ as

$$\frac{V_0}{N}k_BTL_c^{\alpha\beta}=\left[\mathbf{b}^{\alpha}_{\chi_0}|\mathbf{b}^{\alpha}_{\phi_0}\right]\left[\begin{array}{cc}\overline{\mathbf{g}^1} & \overline{\mathbf{g}^3}^T\\ \overline{\mathbf{g}^3} & \overline{\mathbf{g}^2}\end{array}\right]\left[\mathbf{b}^{\beta}_{\chi_0}|\mathbf{b}^{\beta}_{\phi_0}\right]^T \tag{38}$$

where the indices χ_0 and ϕ_0 have the same meaning as in Equation (27) and the symmetrised Green's function elements are obtained by symmetrising the reduced Green's function in Equation (28) as

$$\overline{g^1}_{\mathbf{u}_\mathrm{s}\mathbf{R}_\mathrm{d}\mathbf{u}_\mathrm{d}\mathbf{o}_\mathrm{d},\mathbf{u}'_\mathrm{s}\mathbf{R}'_\mathrm{d}\mathbf{u}'_\mathrm{d}\mathbf{o}'_\mathrm{d}}=\left(\frac{p^0_{\mathbf{0}\mathbf{u}_\mathrm{s}\mathbf{R}_\mathrm{d}\mathbf{u}_\mathrm{d}\mathbf{o}_\mathrm{d}}}{p^0_{\mathbf{0}\mathbf{u}'_\mathrm{s}\mathbf{R}'_\mathrm{d}\mathbf{u}'_\mathrm{d}\mathbf{o}'_\mathrm{d}}}\right)^{\frac{1}{2}}\overline{G^1}_{\mathbf{u}_\mathrm{s}\mathbf{R}_\mathrm{d}\mathbf{u}_\mathrm{d}\mathbf{o}_\mathrm{d},\mathbf{u}'_\mathrm{s}\mathbf{R}'_\mathrm{d}\mathbf{u}'_\mathrm{d}\mathbf{o}'_\mathrm{d}} \tag{39a}$$

$$\overline{g^2}_{\mathbf{u}_\mathrm{m}\mathbf{o}_\mathrm{m},\mathbf{u}'_\mathrm{m}\mathbf{o}'_\mathrm{m}}=\left(\frac{p^0_{\mathbf{0}\mathbf{u}_\mathrm{m}\mathbf{o}_\mathrm{m}}}{p^0_{\mathbf{0}\mathbf{u}'_\mathrm{m}\mathbf{o}'_\mathrm{m}}}\right)^{\frac{1}{2}}\overline{G^2}_{\mathbf{u}_\mathrm{m}\mathbf{o}_\mathrm{m},\mathbf{u}'_\mathrm{m}\mathbf{o}'_\mathrm{m}} \tag{39b}$$

$$\overline{g^3}_{\mathbf{u}_\mathrm{m}\mathbf{o}_\mathrm{m},\mathbf{u}_\mathrm{s}\mathbf{R}_\mathrm{d}\mathbf{u}_\mathrm{d}\mathbf{o}_\mathrm{d}}=\left(\frac{p^0_{\mathbf{0}\mathbf{u}_\mathrm{m}\mathbf{o}_\mathrm{m}}}{p^0_{\mathbf{0}\mathbf{u}_\mathrm{s}\mathbf{R}_\mathrm{d}\mathbf{u}_\mathrm{d}\mathbf{o}_\mathrm{d}}}\right)^{\frac{1}{2}}\overline{G^3}_{\mathbf{u}_\mathrm{m}\mathbf{o}_\mathrm{m},\mathbf{u}_\mathrm{s}\mathbf{R}_\mathrm{d}\mathbf{u}_\mathrm{d}\mathbf{o}_\mathrm{d}} \tag{39c}$$

As in Equation (28), the blocks in Equations (39a), and (39c) are infinite dimensional. Thus, we cannot evaluate the matrix elements in Equation (39) directly. As discussed in the previous section, however, in Equation (38), we need to consider contributions from only complex states with the pure dumbbell within the kinetic shell, and thus we only need to compute those elements of these two blocks that have these complex states in their indices. In the next few sections, we'll discuss how to compute these elements. The relationship at the heart of this procedure is the inverse relationship between the reduced Green's function and transition rate matrix in Equation (29), which using their symmetrised forms can be written as

$$\left[\begin{array}{cc}\overline{\mathbf{g}^1} & \overline{\mathbf{g}^3}^T\\ \overline{\mathbf{g}^3} & \overline{\mathbf{g}^2}\end{array}\right]=\left[\begin{array}{cc}\overline{\mathbf{\Omega}^1} & \overline{\mathbf{\Omega}^3}^T\\ \overline{\mathbf{\Omega}^3} & \overline{\mathbf{\Omega}^2}\end{array}\right]^{-1} \tag{40}$$

Here, the blocks of the symmetrised transition rate matrix on the right hand side are obtained by symmetrising the blocks in Equation (30) using the same probability square root factors in Equation (39).

2.6. Green's function calculation

To compute the required elements of the Green's function in Equation (40), we follow the Dyson equation approach for infinitely large crystalline systems analogous to the case of vacancies in [42]. This approach is based on the fact that in the complex diffusion subspace, since the solid is infinitely large, most of the transitions correspond to pure dumbbell jumps without the influence of the solute, and local modification to these pure dumbbell transition rates occur only for a few transitions involving pure dumbbell jumps within the kinetic shell, extending up to a few nearest neighbours from the solute at most. Thus, we can separate the transition rate matrix on the right hand side of Equation (40) into two contributions: one that contains only pure dumbbell transition rates between complex states without any solute interaction accounted for, and a correction that only locally corrects the first term for complex states in the kinetic shell. This correction term is therefore extremely sparse and as we shall see, it allows us to compute the required Green's function sums in Equation (39) directly. To this end, we first do this separation and write the reduced symmetrised transition rate matrix as

$$\begin{bmatrix} \overline{\boldsymbol{\Omega}^1} & \overline{\boldsymbol{\Omega}^3}^T \\ \overline{\boldsymbol{\Omega}^3} & \overline{\boldsymbol{\Omega}^2} \end{bmatrix} = \underbrace{\begin{bmatrix} \overline{\boldsymbol{\Omega}^0} & \overline{\mathbf{0}} \\ \mathbf{0} & \overline{\boldsymbol{\Omega}^2} \end{bmatrix}}_{\boldsymbol{\Omega}_{02}} + \underbrace{\begin{bmatrix} \delta\overline{\boldsymbol{\Omega}^1} & \overline{\boldsymbol{\Omega}^3}^T \\ \overline{\boldsymbol{\Omega}^3} & \mathbf{0} \end{bmatrix}}_{\boldsymbol{\Omega}_{\mathrm{cor}}} \tag{41}$$

and then write Equation (40) as the Dyson equation

$$\begin{bmatrix} \overline{\mathbf{g}^1} & \overline{\mathbf{g}^3}^T \\ \overline{\mathbf{g}^3} & \overline{\mathbf{g}^2} \end{bmatrix} = \left(\mathbf{1} + \boldsymbol{\Omega}_{02}{}^{-1}\boldsymbol{\Omega}_{\mathrm{cor}}\right)^{-1}\boldsymbol{\Omega}_{02}{}^{-1} \tag{42}$$

The matrix block $\overline{\boldsymbol{\Omega}^0}$ in $\boldsymbol{\Omega}_{02}$ in Equation (41) includes just pure dumbbell transition rates without accounting for any solute interaction. It has elements of the form

$$\begin{aligned} \overline{\Omega^0}_{\mathbf{u}_\mathrm{s}\mathbf{R}_\mathrm{d}\mathbf{u}_\mathrm{d}\mathbf{o}_\mathrm{d},\mathbf{u}'_\mathrm{s}\mathbf{R}'_\mathrm{d}\mathbf{u}'_\mathrm{d}\mathbf{o}'_\mathrm{d}} &= \delta(\mathbf{u}'_\mathrm{s} - \mathbf{u}_\mathrm{s})\left(\frac{p^0_{\mathbf{0}\mathbf{u}_\mathrm{d}\mathbf{o}_\mathrm{d}}}{p^0_{\mathbf{0}\mathbf{u}'_\mathrm{d}\mathbf{o}'_\mathrm{d}}}\right)^{\frac{1}{2}} W^{0,d}_{\mathbf{R}_\mathrm{d}\mathbf{u}_\mathrm{d}\mathbf{o}_\mathrm{d},\mathbf{R}'_\mathrm{d}\mathbf{u}'_\mathrm{d}\mathbf{o}'_\mathrm{d}} \\ &= \delta(\mathbf{u}'_\mathrm{s} - \mathbf{u}_\mathrm{s})\Omega^{0,d}_{\mathbf{R}_\mathrm{d}\mathbf{u}_\mathrm{d}\mathbf{o}_\mathrm{d},\mathbf{R}'_\mathrm{d}\mathbf{u}'_\mathrm{d}\mathbf{o}'_\mathrm{d}} \end{aligned} \tag{43}$$

where $\boldsymbol{\Omega}^{\mathbf{0,d}}$ is the symmetrised transition rate matrix of a pure dumbbell in a solid without any other defect in it. The matrix block $\overline{\boldsymbol{\Omega}^2}$ block is the finite-dimensional mixed dumbbell subspace part of the total reduced transition matrix. Note that in addition to mixed dumbbell transition rates, the diagonal elements of $\overline{\boldsymbol{\Omega}^2}$ also contain the escape rates due to mixed dumbbell annihilation(ω^3 jumps) as per the sum rule in Equation (4), and hence this block is invertible. The matrix $\boldsymbol{\Omega}_{\mathrm{cor}}$ corrects $\boldsymbol{\Omega}_{02}$ by putting in the effect of solute-pure dumbbell interactions on the complex subspace transition rates, and mixed dumbbell formation and annihilation rates in the block $\delta\overline{\boldsymbol{\Omega}^1} = \overline{\boldsymbol{\Omega}^1} - \overline{\boldsymbol{\Omega}^0}$ and the off-diagonal blocks respectively. Note that, $\delta\overline{\boldsymbol{\Omega}^1}$ contains the escape rates due to ω^4 jumps jumps in its diagonal elements as well.

To compute the reduced symmetrised Green's function in Equation (42), we therefore need to invert $\mathbf{\Omega}_{02}$, which we write as

$$\begin{bmatrix} \overline{\mathbf{g^{00}}} & \mathbf{0} \\ \mathbf{0} & \overline{\mathbf{g^{02}}} \end{bmatrix} = \begin{bmatrix} \overline{\mathbf{\Omega^0}} & \mathbf{0} \\ \mathbf{0} & \overline{\mathbf{\Omega^2}} \end{bmatrix}^{-1} \tag{44}$$

The lower-right diagonal block $\overline{\mathbf{g^{02}}}$ is finite-dimensional and therefore can be computed by direct inversion, $\overline{\mathbf{g^{02}}} = (\overline{\mathbf{\Omega^2}})^{-1}$. We then note that the block $\delta\overline{\mathbf{\Omega^1}}$ is highly sparse and contains non-zero elements only between complex states within the kinetic shell. Similarly, the blocks $\overline{\mathbf{\Omega^4}}$ and $\overline{\mathbf{\Omega^3}}$ are also non-zero only for some complex states within the kinetic shell, since mixed dumbbell formation (annihilation) jumps cannot be executed from (to) complex states outside the kinetic shell. Due to this sparsity, an infinite series expansion of $(\mathbf{1} + \mathbf{\Omega_{02}}^{-1}\mathbf{\Omega_{cor}})^{-1}$ can be used to show that we only need to compute elements of $\overline{\mathbf{g^{00}}}$ between complex states with the pure dumbbell within the kinetic shell to be able to compute the elements of the blocks $\overline{\mathbf{g^1}}$ (Equation (39a)) and $\overline{\mathbf{g^3}}$ (Equation (39c)) containing these states in their indices. As discussed in the previous sections, these are the only matrix elements from these blocks that we will need to compute to evaluate the correlated contribution to the transport coefficient. To compute these elements of $\overline{\mathbf{g^{00}}}$, we use the inversion method described in detail in [42] and briefly outlined in the next section. It involves Fourier transforming the symmetrised matrix $\overline{\mathbf{\Omega}^0}$ and evaluating its inverse in Fourier space, and then transforming the inverse back to real space.

2.7. Green's function for pure dumbbell states

To compute the upper diagonal block elements in Equation (44), we first note from Equation (43) that with respect to $\mathbf{u}_\mathrm{s}$, the matrix $\overline{\mathbf{\Omega^0}}$ (and therefore $\overline{\mathbf{g^{00}}}$) is block diagonal, and since we don't account for solute interactions, all these blocks are the same. Thus, it suffices to compute just one block of $\overline{\mathbf{g^{00}}}$ for some given $\mathbf{u}_\mathrm{s}$. We can thus remove $\mathbf{u}_\mathrm{s}$ from our indexing and write

$$\overline{\mathbf{g^{00}}}_{\mathbf{u}_\mathrm{s}\mathbf{R}_\mathrm{d}\mathbf{u}_\mathrm{d}\mathbf{o}_\mathrm{d},\mathbf{u}'_\mathrm{s}\mathbf{R}'_\mathrm{d}\mathbf{u}'_\mathrm{d}\mathbf{o}'_\mathrm{d}} = g^{0,d}_{\mathbf{R}_\mathrm{d}\mathbf{u}_\mathrm{d}\mathbf{o}_\mathrm{d},\mathbf{R}'_\mathrm{d}\mathbf{u}'_\mathrm{d}\mathbf{o}'_\mathrm{d}} = [\Omega^{0,d}]^{-1}_{\mathbf{R}_\mathrm{d}\mathbf{u}_\mathrm{d}\mathbf{o}_\mathrm{d},\mathbf{R}'_\mathrm{d}\mathbf{u}'_\mathrm{d}\mathbf{o}'_\mathrm{d}} \tag{45}$$

We then follow an analogue of the procedure in [42] for vacancies to calculate the matrix elements of $\mathbf{g^{0,d}}$. The first step in the procedure is to solve the eigenvalue equation

$$\sum_{\mathbf{u}'_\mathrm{d},\mathbf{o}'_\mathrm{d}} \left(\sum_{\mathbf{R}'_\mathrm{d}} \Omega^{0,d}_{\mathbf{0}\mathbf{u}_\mathrm{d}\mathbf{o}_\mathrm{d},\mathbf{R}'_\mathrm{d}\mathbf{u}'_\mathrm{d}\mathbf{o}'_\mathrm{d}} \right) s^a_{\mathbf{u}'_\mathrm{d}\mathbf{o}'_\mathrm{d}} = r^a s^a_{\mathbf{u}_\mathrm{d}\mathbf{o}_\mathrm{d}} \tag{46}$$

for eigenvalues r^a and eigenvectors $\mathbf{s}^a$. $\mathbf{\Omega^{0,d}}$ is a symmetric negative semi-definite matrix [26], and hence the (normalized) eigenvectors $\mathbf{s}^a$ are orthonormal. This allows us to write the Fourier transform for $\mathbf{\Omega}^{\mathbf{0,d}}$ using rotated orthonormal basis functions of the form $\frac{1}{\sqrt{N}} s^a_{\mathbf{u}_\mathrm{d}\mathbf{o}_\mathrm{d}} \exp\left[i\mathbf{q}\cdot(\mathbf{R}_\mathrm{d}+\mathbf{u}_\mathrm{d})\right]$ as

$$\widetilde{\Omega}_{a,b}(\mathbf{q},\mathbf{q}') = \frac{1}{N}\sum_{\mathbf{R}_\mathrm{d}\mathbf{u}_\mathrm{d}\mathbf{o}_\mathrm{d},\mathbf{R}'_\mathrm{d}\mathbf{u}'_\mathrm{d}\mathbf{o}'_\mathrm{d}} e^{-i\mathbf{q}\cdot(\mathbf{R}_\mathrm{d}+\mathbf{u}_\mathrm{d})} s^a_{\mathbf{u}_\mathrm{d}\mathbf{o}_\mathrm{d}} \Omega^{0,d}_{\mathbf{R}_\mathrm{d}\mathbf{u}_\mathrm{d}\mathbf{o}_\mathrm{d},\mathbf{R}'_\mathrm{d}\mathbf{u}'_\mathrm{d}\mathbf{o}'_\mathrm{d}} s^b_{\mathbf{u}'_\mathrm{d}\mathbf{o}'_\mathrm{d}} e^{i\mathbf{q}'\cdot(\mathbf{R}'_\mathrm{d}+\mathbf{u}'_\mathrm{d})} \tag{47}$$

where $\mathbf{q}$ and $\mathbf{q}'$ are reciprocal space vectors in the first Brillouin zone. Using translational invariance in $\mathbf{\Omega}^{\mathbf{0,d}}$, this can be written as

$$\widetilde{\Omega}_{a,b}(\mathbf{q},\mathbf{q}') = \delta(\mathbf{q}-\mathbf{q}')\widetilde{\Omega}_{a,b}(\mathbf{q}) \tag{48}$$

where

$$\widetilde{\Omega}_{a,b}(\mathbf{q}) = \sum_{\mathbf{u}_\mathrm{d},\mathbf{o}_\mathrm{d},\mathbf{R}'_\mathrm{d}\mathbf{u}'_\mathrm{d}\mathbf{o}'_\mathrm{d}} s^a_{\mathbf{u}_\mathrm{d}\mathbf{o}_\mathrm{d}} \Omega^{0,d}_{\mathbf{0}\mathbf{u}_\mathrm{d}\mathbf{o}_\mathrm{d},\mathbf{R}'_\mathrm{d}\mathbf{u}'_\mathrm{d}\mathbf{o}'_\mathrm{d}} s^b_{\mathbf{u}'_\mathrm{d}\mathbf{o}'_\mathrm{d}} e^{i\mathbf{q}\cdot(\mathbf{R}'_\mathrm{d}+\mathbf{u}'_\mathrm{d}-\mathbf{u}_\mathrm{d})} \tag{49}$$

We then evaluate $\widetilde{\mathbf{g}}(\mathbf{q}) = \widetilde{\Omega}^{-1}(\mathbf{q})$, the Fourier transform of $\mathbf{g}^{\mathbf{0,d}}$, and use an inverse transformation to get the elements of $\mathbf{g}^{\mathbf{0,d}}$ as

$$g^{0,d}_{\mathbf{R}_\mathrm{d}\mathbf{u}_\mathrm{d}\mathbf{o}_\mathrm{d},\mathbf{R}'_\mathrm{d}\mathbf{u}'_\mathrm{d}\mathbf{o}'_\mathrm{d}} = \frac{V_0}{N}\int_{BZ}\frac{\mathrm{d}\mathbf{q}}{(2\pi)^3} e^{i\mathbf{q}\cdot(\mathbf{R}'_\mathrm{d}+\mathbf{u}'_\mathrm{d}-\mathbf{R}_\mathrm{d}-\mathbf{u}_\mathrm{d})} \sum_{a,b} s^a_{\mathbf{u}_\mathrm{d},\mathbf{o}_\mathrm{d}} \widetilde{g}_{a,b}(\mathbf{q}) s^b_{\mathbf{u}'_\mathrm{d},\mathbf{o}'_\mathrm{d}} \tag{50}$$

where the integral is over the first Brillouin zone and $\frac{V_0}{N}$ is the unit cell volume. $\widetilde{\mathbf{g}}(\mathbf{q})$ is computed in a block-wise manner which we next discuss briefly. We note that for an ergodic system, Equation (46) gives an eigenvalue of zero, which we identify as $r^0 = 0$. Corresponding to this eigenvalue, the eigenvector $\mathbf{s}^0$ has the square roots of the probabilities of the pure dumbbell states within a unit cell as its components, *i.e.*, $s^0_{\mathbf{u}_\mathrm{d}\mathbf{o}_\mathrm{d}} = (p^0_{\mathbf{u}_\mathrm{d}\mathbf{o}_\mathrm{d}})^{\frac{1}{2}}$, where

$$p^0_{\mathbf{0}\mathbf{u}_\mathrm{d}\mathbf{o}_\mathrm{d}} = \frac{e^{-\Delta E_f(\mathbf{0}\mathbf{u}_\mathrm{d}\mathbf{o}_\mathrm{d})/k_BT}}{\sum_{\mathbf{u}_\mathrm{d}\mathbf{o}_\mathrm{d}} e^{-\Delta E_f(\mathbf{0}\mathbf{u}_\mathrm{d}\mathbf{o}_\mathrm{d})/k_BT}} \tag{51}$$

We then write $\widetilde{\mathbf{\Omega}}(\mathbf{q})$ in a blocked structure as follows:

$$\widetilde{\mathbf{\Omega}}(\mathbf{q}) = \begin{bmatrix} \mathbf{DD}(\mathbf{q}) & \mathbf{DR}(\mathbf{q}) \\ \mathbf{RD}(\mathbf{q}) & \mathbf{RR}(\mathbf{q}) \end{bmatrix} \tag{52}$$

where $\mathbf{DD}(\mathbf{q})$ is a 1×1 matrix, corresponding to $a = b = 0$ in Equation (49). The block $\mathbf{RD}(\mathbf{q})$ is a column vector containing elements with $a \neq 0$ and $b = 0$. $\mathbf{DR}(\mathbf{q})$ is the complex conjugate transpose of $\mathbf{RD}(\mathbf{q})$, and $\mathbf{RR}(\mathbf{q})$ contains all remaining elements with $a \neq 0$ and $b \neq 0$ in Equation (49). The block inversion of $\widetilde{\mathbf{\Omega}}(\mathbf{q})$ then becomes exactly the same procedure as for vacancy-mediated diffusion in [42], which we describe in brief below.

We first employ a coordinate transformation in reciprocal space to make the Schur complement of the $\mathbf{RR}(\mathbf{q})$ block

$$\mathbf{D}(\mathbf{q}) = \mathbf{DD}(\mathbf{q}) - \mathbf{DR}(\mathbf{q})\left[\mathbf{RR}(\mathbf{q})\right]^{-1}\mathbf{RD}(\mathbf{q}) \tag{53}$$

isotropic in its leading order term.

To the leading order in $\mathbf{q}$, $\mathbf{D}(\mathbf{q})$ is given by

$$\mathbf{D}(\mathbf{q}) = -\mathbf{q}\cdot\mathbf{D}^{\mathrm{d}}\cdot\mathbf{q} + O(q^4) \tag{54}$$

where $\mathbf{D}^{\mathrm{d}}$ is the diffusivity tensor of a bare dumbbell diffusing in the lattice (without any solute) given by

$$\begin{aligned}\mathbf{D}^{\mathrm{d}} = {} & \frac{1}{2}\sum_{\substack{\mathbf{u}_{\mathrm{d}},\mathbf{o}_{\mathrm{d}}\\ \mathbf{u}'_{d},\mathbf{o}'_{d}}}\sum_{\mathbf{R}'_{d}} p^{0}_{\mathbf{0u}_{\mathrm{d}}\mathbf{o}_{\mathrm{d}}} W^{0,d}_{\mathbf{0u}_{\mathrm{d}}\mathbf{o}_{\mathrm{d}},\mathbf{R}'_{\mathrm{d}}\mathbf{u}'_{\mathrm{d}}\mathbf{o}'_{\mathrm{d}}}\,\delta\mathbf{x}^{A}(\mathbf{0u}_{\mathrm{d}}\mathbf{o}_{\mathrm{d}}\to\mathbf{R}'_{\mathrm{d}}\mathbf{u}'_{\mathrm{d}}\mathbf{o}'_{\mathrm{d}})\otimes\delta\mathbf{x}^{A}(\mathbf{0u}_{\mathrm{d}}\mathbf{o}_{\mathrm{d}}\to\mathbf{R}'_{\mathrm{d}}\mathbf{u}'_{\mathrm{d}}\mathbf{o}'_{\mathrm{d}})\\ & + \sum_{\mathbf{u}_{\mathrm{d}}\mathbf{o}_{\mathrm{d}},\mathbf{u}'_{d}\mathbf{o}'_{d}} \mathbf{b}^{0}_{\mathbf{0u}_{\mathrm{d}}\mathbf{o}_{\mathrm{d}}}\left(\sum_{\alpha>0} s^{\alpha}_{\mathbf{0u}_{\mathrm{d}}\mathbf{o}_{\mathrm{d}}}(r^{\alpha})^{-1}s^{\alpha}_{\mathbf{0u}'_{\mathrm{d}}\mathbf{o}'_{\mathrm{d}}}\right) b^{0}_{\mathbf{0u}'_{\mathrm{d}}\mathbf{o}'_{\mathrm{d}}}\end{aligned} \tag{55}$$

where A denotes the solvent species and $\mathbf{b}^{0}_{\mathbf{0u}_{\mathrm{d}}\mathbf{o}_{\mathrm{d}}}$ is the bias vector of a pure dumbbell given by

$$\mathbf{b}^{0}_{\mathbf{0u}_{\mathrm{d}}\mathbf{o}_{\mathrm{d}}} = \left(\sum_{\mathbf{R}''_{\mathrm{d}},\mathbf{u}''_{\mathrm{d}},\mathbf{o}''_{\mathrm{d}}}\left(p^{0}_{\mathbf{0u}_{\mathrm{d}}\mathbf{o}_{\mathrm{d}}}\right)^{\frac{1}{2}} W^{0,d}_{\mathbf{0u}_{\mathrm{d}}\mathbf{o}_{\mathrm{d}},\mathbf{R}''_{\mathrm{d}},\mathbf{u}''_{\mathrm{d}},\mathbf{o}''_{\mathrm{d}}}\,\delta\mathbf{x}^{A}(\mathbf{0u}_{\mathrm{d}}\mathbf{o}_{\mathrm{d}}\to\mathbf{R}''_{\mathrm{d}},\,\mathbf{u}''_{\mathrm{d}},\,\mathbf{o}''_{\mathrm{d}})\right) \tag{56}$$

$\mathbf{D}^{\mathrm{d}}$ being symmetric and positive definite has an orthogonal set of eigenvectors. We denote its (eigenvalue, eigenvector) pairs as $(d_i, \mathbf{e}_{\mathbf{i}})$, $i \in \{1, 2, 3\}$. Using these eigenpairs of $\mathbf{D}^{\mathrm{d}}$, we transform the reciprocal lattice coordinates $\mathbf{q}$ and the real space coordinates $\mathbf{x}$, using the relations

$$p_i = (d_i)^{\frac{1}{2}}(\mathbf{e}_i\cdot\mathbf{q}),\quad y_i = (d_i)^{\frac{1}{2}}(\mathbf{e}_i\cdot\mathbf{x}),\ \ i \in \{1, 2, 3\} \tag{57}$$

In the transformed coordinates $\mathbf{p}$, the Schur complement in Equation (53) becomes isotropic in leading order and is given by

$$\mathbf{D}(\mathbf{p}) = -p^2 + O(p^4) \tag{58}$$

The Fourier transform of the Green's function in the transformed reciprocal space can then be computed as

$$\tilde{\mathbf{g}}(\mathbf{p}) = \left[\begin{array}{c|c} \mathbf{D}^{-1}(\mathbf{p}) & -\mathbf{D}^{-1}(\mathbf{p})\mathbf{DR}(\mathbf{p})\mathbf{RR}^{-1}(\mathbf{p}) \\ \hline -\mathbf{RR}^{-1}(\mathbf{p})\mathbf{RD}(\mathbf{p})\mathbf{D}^{-1}(\mathbf{p}) & \mathbf{RR}^{-1}(\mathbf{p}) + \mathbf{RR}^{-1}(\mathbf{p})\mathbf{RD}(\mathbf{p})\mathbf{D}^{-1}(\mathbf{p})\mathbf{DR}(\mathbf{p})\mathbf{RR}^{-1}(\mathbf{p} \end{array}\right. \tag{59}$$

where $\mathbf{D}^{-1}(\mathbf{p})$ and $\mathbf{RR}^{-1}(\mathbf{p})$ are isotropic in their leading order terms, which are $\frac{1}{p^2}$ and $(r^\alpha)^{-1}\delta_{\alpha\beta}$ respectively. Computing $\widetilde{\mathbf{g}}$ in reciprocal space in this block-wise manner is necessary as it allows us to handle complications with poles and discontinuities that arise as $\mathbf{p}\rightarrow\mathbf{0}$ during inverse Fourier transformation. In this limit, the $\mathbf{D}^{-1}(\mathbf{p})$ block has a second-order pole, while the other blocks have poles and discontinuities depending on the direction of approach towards the origin (see section 2.1 in [42] for details). To mitigate these problems, the blocks of $\widetilde{\mathbf{g}}(\mathbf{p})$ are written as a sum of terms that have the same poles and discontinuities as $\mathbf{p}\rightarrow\mathbf{0}$ as the corresponding blocks in $\widetilde{\mathbf{g}}(\mathbf{p})$ but can be analytically inverse transformed, and a remaining correction term called the semi-continuum piece which is the difference of the sum of these terms from $\widetilde{\boldsymbol{\Omega}}^{-1}$ at all points in the first Brillouin zone.

The semi-continuum piece is a smooth function in the first Brillouin zone, and its inverse transform is computed using numerical integration in the first Brillouin zone. In Appendix 4, we have shown that the resulting estimated integration errors in $\overline{\mathbf{g}^{\mathbf{00}}}$ can be made as small as $\sim 10^{-8}$ with grid sizes small enough for computation times of a few seconds. Moreover, we note that the evaluation of $\overline{\mathbf{g}^{\mathbf{00}}}$ is independent of the solute. So, elements of this block can be reused for multiple solutes. This makes the present method highly suitable for computations such as uncertainty quantification [43] and other such high-throughput studies, where transport coefficients for several different solutes need to be computed under varying conditions.

2.8. Symmetry grouping of states

To accelerate the computation of the transport coefficients, we adopt a strategy to group states by symmetry in a manner similar to the case of vacancy-mediated diffusion as described in [42]. We start by forming *state orbits* (analogous to ‘crystal stars’ in [42]), which are sets of states such that any two states in the same state orbit are related by a symmetry operation. All states in the same orbit will then have the same formation energy and hence the same probability. We therefore need only compute these quantities for a single state in an orbit. From state orbits, we can next form *state-vector orbits* (analogous to ‘vector stars’ in [42]). A state-vector orbit is a set of (state (n), unit vector ($\mathbf{a}_n$)) tuples, so that any two such tuples in the same state-vector orbit are related to each other by symmetry in the sense that the symmetry operation that transforms the state n to n', also transforms the unit vector $\mathbf{a}_n$ to $\mathbf{a}_{n'}$. This also implies that if a symmetry operation leaves a state unchanged, it also leaves the unit vector associated with it unchanged. We then define as S_n the subspace of real space that corresponds to the space of fixed vector points of the little group of a state n. Corresponding to each state orbit, there will be as many state-vector orbits as the dimensionality of S_n for any representative state n from that orbit. It also follows that if two states n and n' are related by symmetry, then S_n and $S_{n'}$ will also be related by the same symmetry operation. It's important to note that vector-valued state functions must map on to S_n when evaluated on state n.

Now, no two state-vector orbits have a common (state, unit vector) tuple, and every state n must occur in as many state-vector orbits as the dimensionality of S_n (associated with a different independent basis vector for S_n each time). These facts imply that the state-vector orbits can be used to construct a complete set of basis functions to expand vector-valued functions of states. For every state-vector orbit (denoted by ξ), we can define such a basis function $\boldsymbol{\lambda}_\xi$ as

$$\boldsymbol{\lambda}_\xi(n) = \frac{1}{\sqrt{|\xi|}} \sum_{(n',\mathbf{a}_{n'})\in\xi} \mathbf{a}_{n'} \delta_{n'}(n) \tag{60}$$

where $|\xi|$ is the number of unique (state, unit vector) tuples in the state-vector orbit and

$$\delta_{n'}(n) = \begin{cases} 1 & \text{if } n' = n \\ 0 & \text{otherwise} \end{cases} \tag{61}$$

These vector functions can then be used to represent vector-valued state functions. For example, the velocity vector of a species α in state n can be written as

$$\mathbf{v}_n^\alpha = \sum_\xi v_\xi^\alpha \boldsymbol{\lambda}_\xi(n) \tag{62}$$

where

$$v_\xi^\alpha = \frac{1}{\sqrt{|\xi|}} \sum_{(n',\mathbf{a}_{n'})\in\xi} \mathbf{v}_{n'}^\alpha \cdot \mathbf{a}_{n'} \tag{63}$$

These basis functions can also be used to represent matrices such as the transition rate matrix as:

$$\begin{aligned} W_{\xi\xi'} &= \frac{1}{\sqrt{|\xi||\xi'|}} \sum_{n,n'} W_{nn'} \boldsymbol{\lambda}_\xi(n) \cdot \boldsymbol{\lambda}_{\xi'}(n') \\ &= \frac{1}{\sqrt{|\xi||\xi'|}} \sum_{(n,\mathbf{a}_n)\in\xi} \sum_{(n',\mathbf{a}_{n'})\in\xi'} W_{nn'} \mathbf{a}_n \cdot \mathbf{a}_{n'} \end{aligned} \tag{64}$$

We can also calculate the Green's function by evaluating the Dyson equation in the basis of the state-orbit basis functions. To do this, we use equations similar to Equation (64) above to construct representations of various pieces of the Dyson equation shown in Equations (42) and (44). In this representation, there are fewer quantities to be calculated. For example, in Equation (63), the term $\mathbf{v}_{n'}^\alpha \cdot \mathbf{a}_{n'}$ is the same for all $(n', \mathbf{a}_{n'}) \in \xi$ since symmetry operations that rotate both $\mathbf{v}_{n'}^\alpha$ and $\mathbf{a}_{n'}$ simultaneously will leave their inner product unchanged. For every vector orbit, this inner product then only needs to be computed once for a representative (state, unit vector) pair. Similarly, instead of computing the transition rates for all jumps individually, we can form orbits of transitions, such that if a pair of states n_1 and n_2 are transformed by the same symmetry operation to produce the states n_3 and n_4 respectively in the same transition orbit, then $W_{n_1,n_2} = W_{n_3,n_4}$. We therefore need to compute the rate only once for a representative from each group of transitions related by symmetry. A similar method may be employed to reduce the number of elements of $\overline{\mathbf{g^{00}}}$ in the Dyson equation that need to be calculated explicitly, by grouping together symmetrically related pairs of complex states (we only need those with the pure dumbbell within the kinetic shell). For systems where a lot of states are related to each other by symmetry, the number of state and state-vector orbits can be considerably fewer than the number of states so that this approach can allow substantial reduction in the cost of computing the transport coefficients.

2.9. Data for alloy simulation

To compare our implemented Green's function approach with existing results in the literature, as well as to gain additional insights into dumbbell mediated solute diffusion, we compute transport coefficients for two types of alloys using energetic data already available in the literature. For dilute BCC Fe-S alloys (S = Cr, Mn, Cu, Ni, Si), we used the energetic data available in the database in [47], based on the calculations in [48]. In these calculations, energetic interactions were considered up to the fifth-nearest-neighbour separation between solutes and pure dumbbells in complex states. For all the dilute alloys, the 60° roto-translation mechanism was considered for all the jump types in Figure 1. In addition, migration barrier data were also available and considered for pure and mixed dumbbell jumps (ω^0, ω^1 and ω^2 jumps) via rigid translation in the Fe-Mn, Fe-Cu, Fe-Ni and Fe-Si dilute alloys and pure dumbbell on-site 60° rotations were also considered for the same four alloys. Also, on-site 60° rotations for mixed dumbbells were considered for the Fe-Mn alloy. The transition rates for these mechanisms were computed from the migration barriers as

$$W = \nu e^{-\frac{\Delta E_{mig}}{k_B T}} \tag{65}$$

where ν is the attempt frequency, and $\Delta E_{mig} = E_{TS} - E_i$, with E_{TS}, the transition state energy being the same for forward and reverse jumps, thus preserving detailed balance. E_i is the energy of the initial state.

We used the data available in [19,49] for calculations on dilute FCC Ni-S alloys (S = Cr, Fe). In these calculations, only nearest neighbour solute-dumbbell energetic interactions were considered in complex states. The

Table 1. Binding energies (in eV) of solute(S)-dumbbell configurations in FCC Ni, as defined in [19], calculated from jump migration barriers in Table D.4 in [19], using detailed balance. Negative energies indicate attraction. The binding energies indicate the relative stabilities of the states compared to a far-separated solute-⟨100⟩ pure dumbbell complex state.

Configuration	S = Cr	S = Fe
Ni-S mixed dumbbell	−0.42	0.11
a-type	−0.11	0.06
b-type	−0.11	−0.02

jump mechanisms considered for both pure and mixed dumbbell diffusion are the 90° roto-translation mechanism along with on-site rotations. An important point needs to be addressed regarding the solute binding energies in [19], which is that they do not satisfy detailed balance between forward and reverse jumps. From the migration barriers for the various jump mechanisms given in Table D.4 of [19], and the formation energy of the pure Ni-Ni dumbbells (reported as 4.07 eV in [19]), we computed and used the binding energies such that the transition state energies are the same for forward and reverse jumps. These binding energies are shown in Table 1. This is also discussed in [49] and similar binding energies are reported there in Table 3.15. We identify a maximum deviation of 0.08 eV between the two sets of binding energies. In Table 1, an 'a-type' complex (following the notation in [19]) is a nearest neighbour solute-pure dumbbell complex, formed such that the pure dumbbell can execute a ω^4 jump via the roto-translation mechanism to form a mixed dumbbell. A 'b-type' orientation is also a nearest neighbour solute-pure dumbbell complex, but from which no such ω^4 jump can occur.

As in [19], temperature-dependent electronic contributions were also considered for the migration rates using a Sommerfeld approximation to the transition rates. We also use the approximation in [19] that the rate of every jump involving a Ni atom hop, i.e. the ω^0, ω^1, ω^3 and ω^4 jumps have the same electronic contribution to their jump rates. The transition rates then have the form

$$W = \nu E_C(T) e^{-\frac{\Delta E_{mig}}{k_B T}} \tag{66}$$

where E_C is the electronic contribution. As mentioned in [19], however, the largest contributions to the migration rates are the activation energy barriers and not the electronic contributions. We also verified that excluding the latter by setting $E_C(T) = 1$ does not significantly impact our results. We therefore do not go into further details of these contributions. The interested reader is referred to Appendices C.2, D and Table D.4 in [19], for further details and data for these contributions.

3. Results and discussion

3.1. Diffusivities in the dilute limit

In the dilute limit, the transport coefficients in Equation (24) can be written as terms that are simply scaled by the species concentrations as

$$\frac{V_0}{N} k_B T L^{AA} = c_i l_0^{AA} + c_s c_i l_1^{AA} = c_i D^A \tag{67a}$$

$$\frac{V_0}{N} k_B T L^{SS} = c_s c_i l_1^{SS} = c_s D^S \tag{67b}$$

$$\frac{V_0}{N} k_B T L^{AS} = c_s c_i l_1^{AS} \tag{67c}$$

with $\frac{V_0}{N}$ being the volume of a unit cell, and D^α is the commonly used diffusion coefficient, which relates the flux of species α to its own volume concentration gradient. The concentration factors arise from the equilibrium state probabilities (Equations (17) and (18)), and the relationship to the diffusion coefficients comes about as $\nabla\mu = (k_\mathrm{B}T/c)\nabla c$ in the dilute limit. In addition, the use of translation symmetry as mentioned in Equation (A2) and the invariance principle discussed in Section 2.4 would also be required to restrict correlations within the kinetic shell.

In our implementation, we compute l_0^{AA}, l_1^{AA}, l_1^{AS} and l_1^{SS}. The term l_0^{AA} corresponds to the contribution to L^{AA} due to the diffusion of a pure interstitial dumbbell with no solute being present ($\delta W^1 = 0$ for all dumbbell jumps). The contribution by this term does not depend on the solute concentration and scales with only the solvent interstitial concentration c_i. The next term l_1^{AA} consists of the corrections to the first term due to solute-dumbbell interactions and correlations within the kinetic shell, i.e, due to ω^1 jumps with $\delta W^1 \neq 0$, as well as due to ω^2, ω^3 and ω^4 jumps. This correction term, and the terms l_1^{AS} and l_1^{SS}, which also depend on mixed states and solute-dumbbell complex states within the kinetic shell scale with the product $c_s c_i$ to produce the transport coefficients. We next discuss the range of concentrations over which the present model may be valid.

We note that l_1^{AA}, l_1^{AS} and l_1^{SS}, which contain all the correlations contained within the Green's function, are computed based on the diffusion of a single interstitial dumbbell in the presence of a single solute and do not include more complex interactions between more than these two defects. For example, in concentrated irradiated systems, a defect species that arises is a dumbbell involving two solute atoms [14], which we clearly do not consider. Neglecting the effect of such interactions on the jump mechanisms and therefore the Green's function places a limitation on the validity of our model's transport coefficients when compared to values observed in experiment. As a rough approximation, with dumbbell concentrations assumed very low, we can consider the limiting solute concentration for our model to be accurate to be at most $\frac{1}{N_{KS}}$ where N_{KS} is the number of sites within a solute's kinetic shell. Solutes need to be separated far enough for simultaneous interactions between two solutes and a dumbbell to be rare or absent. Furthermore, a mixed dumbbell should also annihilate before reaching the neighborhood of another solute. The next-order correction to the dilute limit will scale as the concentration of solute; it is worth noting however, that even for concentrated systems, dilute limit results have been successfully used to qualitatively explain observed phenomena in irradiated systems [48]. This indicates that the two-body effects between a single solute and a dumbbell are still physically relevant at higher concentrations, though quantitative disagreements are likely to arise.

3.2. Tracer correlation factors

The tracer correlation factor, f, defined as the ratio of the transport coefficient of a chemical tracer atom to its uncorrelated value [50] is a measure of the dependence of successive atomic jumps on each other during diffusion. For a given type of defect that induces a given jump mechanism, it depends only on the underlying crystal structure and the diffusion mechanism induced by the defect and is independent of state energies, jump rates and the lattice parameter of a crystal. We can thus use f as a means of validating our implementation of the Green's function approach by comparing our computed values with those in the literature obtained with other methods. For dumbbell-mediated diffusion in systems with inversion symmetry, f can be written as

$$f = \frac{L^{A^*A^*}}{L^{A^*A}} \tag{68}$$

where A^* corresponds to a chemical tracer atom of the solvent, and A to a solvent atom.

We verified f for three types of dumbbell diffusion mechanisms that are of interest in FCC and BCC (mainly Fe-based) alloys for structural applications in irradiated environments. In Fe-based BCC alloys, the most stable dumbbell configuration has been shown to be $\langle 110\rangle$ oriented dumbbells [15,16]. The dumbbell diffusion mechanisms for which f was calculated in the BCC crystal structure were the $\langle 110\rangle - \langle 110\rangle$ dumbbell transitions to nearest neighbour sites, involving a 60° reorientation of the dumbbell configuration, and rigid translation of a $\langle 110\rangle$ oriented dumbbell to a nearest neighbour site, as shown in Table 2. For FCC systems, the most stable dumbbell configurations have been found to be the $\langle 100\rangle$ oriented dumbbells [17]. The mechanism in FCC systems for which we computed f is the $\langle 100\rangle - \langle 100\rangle$ dumbbell transitions to a nearest neighbour site with 90° reorientation. The results of our calculations are shown in Table 2. These mechanisms are the most favourable dumbbell diffusion mechanisms in these systems [16,39], and have been studied by other authors as well, including those we refer to in Table 2.

Table 2. Tracer correlation factors for dumbbell diffusion mechanisms in FCC and BCC lattices.

Mechanism	BCC ⟨110⟩ ↔ ⟨110⟩ 60° roto-translation 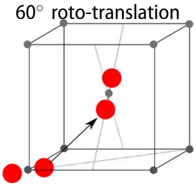	BCC ⟨110⟩ ↔ ⟨110⟩ rigid translation 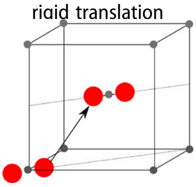	FCC ⟨100⟩ ↔ ⟨100⟩ 90° roto-translation 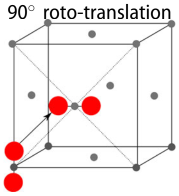
This work	0.412 6434	0.494 3020	0.439 50809
Schuler *et al.* [41]	0.412 6439	0.494 3235	0.439 45498
Bocquet[34] (BCC Only)	0.413 010	0.494 3235	-
Wolff [24]	0.407 ± 0.004	0.475 ± 0.005	0.442 ± 0.004

It can be seen from Table 2 that our results show good agreement with the SCMF results in [41] and with the stochastic ‘Encounter Model’ results in [24], and also for the BCC mechanisms, with the values given in [34] (in [34], we refer to the case when square of the nearest neighbour jump distance is considered to compute the uncorrelated contribution to the tracer transport coefficient instead of average squared displacements of so-called ‘macrojumps’ of the tracer consisting of multiple mixed dumbbell formation, diffusion and annihilation steps). This indicates that our implemented Green’s function approach handles the symmetries of the crystal structures correctly. In Appendix 2, we discuss some special cases that arise in non-ergodic diffusion mechanisms in Table 2 (the FCC 90° roto-translation mechanism and the BCC rigid translation mechanism) and the necessary measures to compute their tracer correlation factors.

3.3. Drag ratios

We next analyse the drag ratios for the dilute BCC Fe-S (S = Cr, Mn, Cu, Ni, Si) and FCC Ni-S (S = Cr, Fe) alloys for dumbbell mediated diffusion. The drag ratio is defined as $\frac{L^{SA}}{L^{SS}}$, where S and A represent solute and solvent species respectively. The sign and magnitude of the drag ratio give the relative direction and amount of diffusion flux of SIAs compared to solute atoms under a solute CPG respectively. As no directional bias is produced in pure dumbbell diffusion by a solute CPG, the drag ratio is governed mainly by mixed dumbbell diffusion. Since the solute and the SIA both move in the same direction during mixed dumbbell diffusion, the sign of the drag ratio always remains positive and its magnitude is greater than or equal to one. The variation of the drag ratio with temperature depends on competing jump mechanisms that affect mixed dumbbell diffusion.

The drag ratios for the Fe-S (S = Cr, Mn, Cu, Ni, Si) alloys are shown in Figure 2. For these alloys, we also show our results in comparison to results

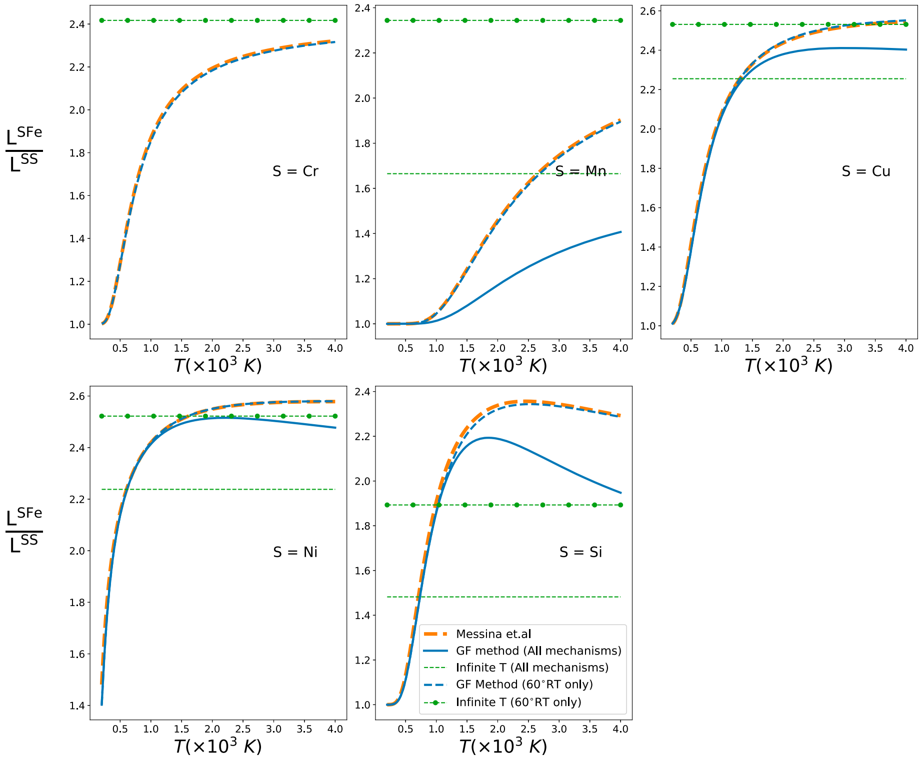

Figure 2. Drag ratios for solutes in BCC iron for dumbbell-mediated diffusion as a function of temperature. Green's function (GF) method results are compared with SCMF results of Messina *et al.* in [47,48] for the 60° roto-translation mechanism (60°RT) showing good agreement for all the solutes. GF method results with all mechanisms for the respective solutes mentioned in [47] are also shown. Values at the infinite temperature limit computed with the Green's function method are indicated with horizontal lines. Increasing drag ratio with temperature indicates higher self-interstitial flux under a solute chemical potential gradient than solute flux. The drag ratios for Cu, Ni and Si are found to exceed the infinite temperature limit at low temperatures, and then decrease towards that limit as temperatures increase.

provided in the database [47] where only the 60° roto-translational mechanism was considered operative. We first note that since the drag ratios are greater than one at almost all temperatures, a higher amount of SIA flux occurs compared to solute flux against the solute CPG direction. We next observe that the BCC Fe alloys show two types of behaviour. In the Fe-Cr and Fe-Mn alloys, the drag ratio increases with temperature monotonically towards the infinite temperature limit. On the other hand, in Fe-Cu, Fe-Ni and Fe-Si, with increasing temperature, the drag ratio first increases and exceeds the infinite temperature limit, reaches a maximum and then decreases towards the infinite temperature limit.

To understand this variation in the behaviour of the drag ratios, we first try to identify the source of the excess SIA flux compared to solutes. Since in our dilute limit model both solute and dumbbell concentrations are fixed, the excess flux of the SIA originates from excess velocity it gains during mixed dumbbell diffusion under a solute CPG. The origin of this excess velocity is schematically shown in Figure 3, with the 60° roto-translation mechanism in BCC alloys as an illustrative example. From the figure, we can see that during diffusion under a solute CPG, a mixed dumbbell alternates between orientations that are geometrically more suited for ω^2 jumps (the '+' orientations) as well as less suited for ω^2 jumps (the '−' orientations) against the solute CPG. If we assume all migration rates to be equal to each other in the absence of any CPG (as they would be for a tracer atom for example), then under a solute CPG mixed dumbbells with '+' orientations will have more propensity to migrate via ω^2 jumps than annihilate via ω^3 jumps, while those with '−' orientations will have more propensity to annihilate than migrate. Since ω^3 jumps have no contribution to solute velocity (as it does not leave the mixed dumbbell site), they provide an excess velocity to the SIA over the solute as they jump to atomic sites against the solute CPG direction from '−' oriented dumbbells, leading to an excess flux over the solutes. Thus L^{SA} becomes greater than L^{SS} and the drag ratio exceeds one.

We use this hypothesis to first qualitatively understand the behaviour of the drag ratios of BCC alloys. For simplicity, we assume that the 60° roto-translation mechanism, being the lowest barrier dumbbell translation mechanism, is the main mechanism of interest. We also assume in our qualitative discussion that the ω^0 and ω^1 rates are the same. As shown in the contour plot to the left of Figure 4, we first try to understand the variation of the drag ratio due to

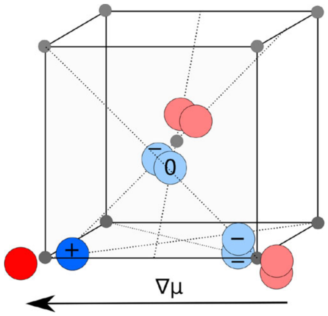

Figure 3. Schematic representation of mixed dumbbell configurations in a BCC crystal that form during diffusion under a solute CPG (applied to the left as shown by the arrow). The red circles represent the self-interstitial atom while the blue circles represent the solute. During diffusion, a mixed dumbbell can form with three types of configurations relative to the CPG direction. The '+' configurations are oriented geometrically for ω^2 jumps strictly to sites against the CPG direction and ω^3 jumps to sites along the CPG. ω^2 jumps from '−' oriented mixed dumbbells are strictly to sites along the CPG, and ω^3 jumps opposite to the CPG. The '0' orientations can geometrically execute these jumps to sites both along or opposite to the CPG direction. Under a solute CPG, the higher propensity of '−' oriented dumbbells to execute ω^3 than ω^2 jumps impart an excess velocity to the self-interstitial atom over the solute in a direction opposite to the CPG.

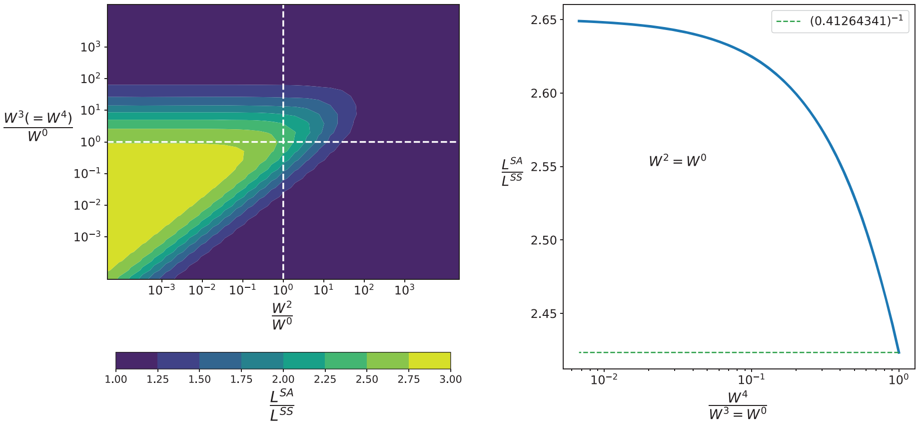

Figure 4. Variation of the drag ratio for a solute (S) in a BCC system under dumbbell-mediated diffusion by the 60° roto-translation mechanism shown in Table 2. From the contour plot on the left, we see that as the ω^3 rate is made much faster (top left region) or much slower (bottom right region) compared to the ω^2 rate, the drag ratio decreases towards 1. The intersection of the two white lines is the tracer condition where all rates are the same. On the right, we see that when the ω^4 rate is slower than the ω^3 rate, the drag ratio (the blue line) is higher and decreases as the ω^4 rate approaches the same value as ω^3, towards the inverse of the tracer correlation factor (indicated by the dotted horizontal line).

competing ω^2 and ω^3 rates. We see that when the ω^2 rate is high and ω^3 rate is low, the drag ratio is lower and close to one. This is because the annihilation of mixed dumbbells with '−' orientations becomes slower compared to migration, leading to the loss of the excess SIA velocity over the solute. This is analogous to the behaviour of Fe-Cr and Fe-Mn alloys at low temperatures, which have ω^2 barriers of 0.241 eV and 0.316 eV and higher ω^3 barriers of 0.365 eV and 0.448 eV respectively. Thus, at low temperatures, the ω^2 rates will be higher than ω^3, leading to a low drag ratio. As the temperature increases, the ω^3 rates start to approach ω^2 rates, so that the excess SIA velocity due to preferred annihilation of '−' oriented dumbbells increases, leading to an increasing drag ratio.

From the same contour plot, we can see that when ω^2 rates are low and ω^3 rates are high, then too, low drag ratios are observed. This is because due to easier mixed dumbbell annihilation, '+' oriented dumbbells also start to annihilate easily, inducing SIA velocity along the solute CPG, and thereby providing opposition to the excess SIA velocity due to preferred annihilation of '−' oriented dumbbells. This is analogous to the low temperature behaviour of Fe-Cu, Fe-Ni and Fe-Si alloys. They have ω^2 barriers of 0.364 eV, 0.464 eV and 0.568 eV, and much lower ω^3 barriers of 0.0 eV, 0.083 eV and 0.069 eV respectively, indicating a higher mixed dumbbell annihilation probability for all mixed dumbbell orientations than migration. With increasing temperature, the relative rate difference between ω^2 and ω^3 jumps starts to decrease in these solutes, leading to increased migration rates of '+' oriented mixed dumbbells aided by the solute CPG compared to annihilation than '−' oriented mixed dumbbells and thus a higher drag ratio.

The subsequent decreasing behaviour of the drag ratios in Fe-Cu, Fe-Ni and Fe-Si alloys with increasing temperatures can be attributed to ω^4 jumps, which have barriers of 0.445 eV, 0.339 eV and 0.345 eV for the three alloys respectively. At low temperatures, therefore, the ω^4 jumps rates would clearly be low compared to ω^3 jump rates, thereby providing an additional bias for SIA motion away from the solute site against the solute CPG direction after annihilation of '−' mixed dumbbells. This is also shown schematically on the plot to the right in Figure 4, where we can see that when the ω^4 rate is lower compared to the ω^3 rate, the drag ratio is higher and as the ω^4 rate approaches the ω^3 rate, the drag ratio decreases towards the limiting value.

Finally, we note that in the dilute Fe alloys the drag ratio also depends on other jump mechanisms in addition to the 60° roto-translation mechanism at high temperatures when they become significant. They also generally show a trend of decreasing the drag ratio for all the solutes compared to only when the 60° roto-translation mechanism is considered. This is because these mechanisms provide additional diffusion pathways for a pure dumbbell to return and form a mixed dumbbell with the solute, as well as more diffusion pathways for the mixed dumbbell itself to diffuse, leading to more solute flux along with SIA under a solute CPG and a lower drag ratio.

It is worth noting here that in the case of vacancy-mediated diffusion, drag ratios can have both positive and negative values and it behaves monotonically with temperature, governed mainly by the jump-rate dependent probabilities of the vacancy to turn around towards the solute site to produce vacancy-solute exchange jumps successively after each jump [51]. On the other hand, the directional nature of the dumbbells, its alignment with the chemical potential gradient and the existence of the additional mixed dumbbell jump mechanisms and their interplay can make the behaviour of the drag ratio non-monotonic with temperature and dumbbell-mediated drag ratios are always positive. We note however that for almost all of the solutes in the Fe-based alloys, these mechanisms start to become significant at temperatures that are too high for relevance in real-world applications.

The drag ratios of the Ni alloys are shown in Figure 5. In Ni-Fe and Ni-Cr alloys, the drag ratio seems to be predominantly controlled by the on-site rotation rates of the mixed dumbbells in agreement with previous results in literature [35]. In Ni-Fe and Ni-Cr, on-site 90° mixed dumbbell rotations have barriers of 0.87 eV and 0.75 eV, while the 90° roto-translation mechanism has a barrier of 0.16 eV and 0.08 eV respectively. Thus, we can expect that at low temperatures, compared to mixed dumbbell roto-translation, on-site rotations will almost never occur. As shown in Figure 6, in such a situation, mixed dumbbell diffusion is geometrically restricted to within octahedral cages [18,35], and unlike the BCC alloys, no long-ranged mixed dumbbell

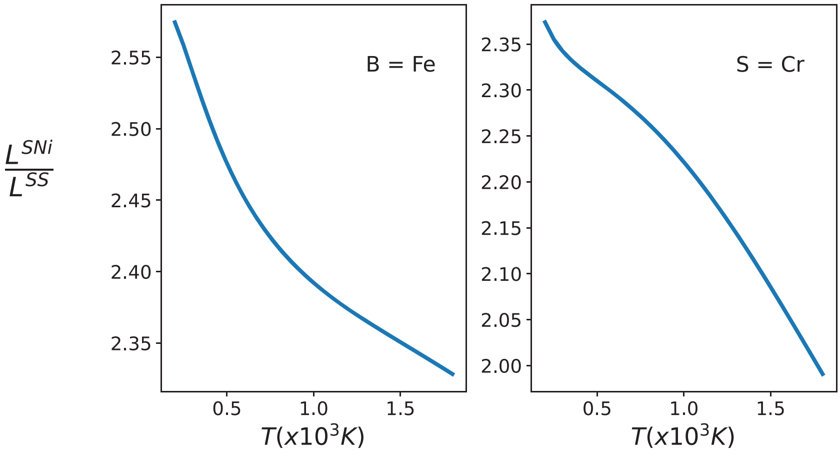

Figure 5. Drag ratios for in dilute Ni-S (S = Fe, Cr) for dumbbell-mediated diffusion computed using the Green's function method. For both Fe and Cr, the drag ratio remains consistently greater than one, indicating greater dependence of solute diffusion on self-interstitial CPG compared to solute CPG. The drag ratio decreases monotonically with increasing temperature because of increasing on-site rotation of mixed dumbbells that facilitate long-ranged diffusion of solutes under a solute CPG, thus increasing L^{SS}.

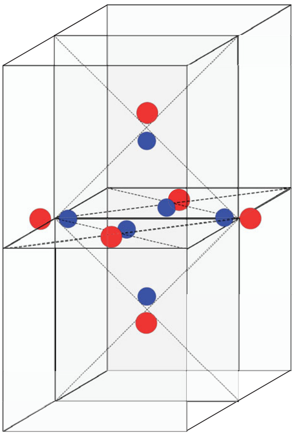

Figure 6. Restriction of ⟨100⟩ oriented mixed dumbbell diffusion within an octahedral cage in an FCC lattice, with 90° roto-translational jumps being the only solute jump mechanism [18,35]. The red atoms represent the solvent self-interstitial atoms and the blue atoms represent the solute. The face centres are indicated via the intersections of the dotted lines running along the face diagonals. Since mixed dumbbell diffusion involves solute atoms jumping from one site to the next to form mixed dumbbells, it can be seen that only mixed dumbbells within an octahedral cage can form from one another via ω^2 jumps occuring via the 90° roto-translational mechanism shown in Table 2 for FCC lattices. The solute atom thus cannot escape this octahedral cage and there is no long-ranged mixed dumbbell diffusion under a solute chemical potential gradient. On-site rotations of the mixed dumbbells can help the solute atom escape the octahedral cage.

diffusion can occur, making L^{SS} smaller than L^{SNi}. As the temperature increases, the on-site rotation rates approach the roto-translation rates, allowing for mixed dumbbell diffusion beyond the octahedral cage leading to higher solute flux. Thus, the drag ratio starts decreasing. This can also be seen in Figure 7, where we artificially keep all jump rates to be the same and only vary the on-site mixed dumbbell rotation rate relative to the roto-translation rate. We can clearly see that the drag ratio for such a situation starts at the inverse of the tracer correlation factor for the 90° roto-translation mechanism and decreases as the on-site rotation rate increases towards 1.0 (as also seen in [35]), analogously to the two FCC alloys.

3.4. Partial diffusion coefficient ratios

We next discuss the Partial Diffusion Coefficient (PDC) ratios for the Fe-S (S = Cr, Mn, Cu, Ni, Si) and Ni-S (S = Fe, Cr) alloys. This ratio is defined as L^{SA}/c_sL^{AA}, where A is the solvent and c_s is the solute concentration. From Equation (67a), since in the dilute limit the contribution by l_1^{AA} is proportional to $\frac{1}{N^2}$, for large N, we can only consider the leading contribution to L^{AA}. The PDC ratio, $L^{SA}/c_sL^{AA} \approx l_1^{SA}/l_0^{AA}$, is then independent of c_s and c_i and only depends on correlation effects between a single solute and a single dumbbell.

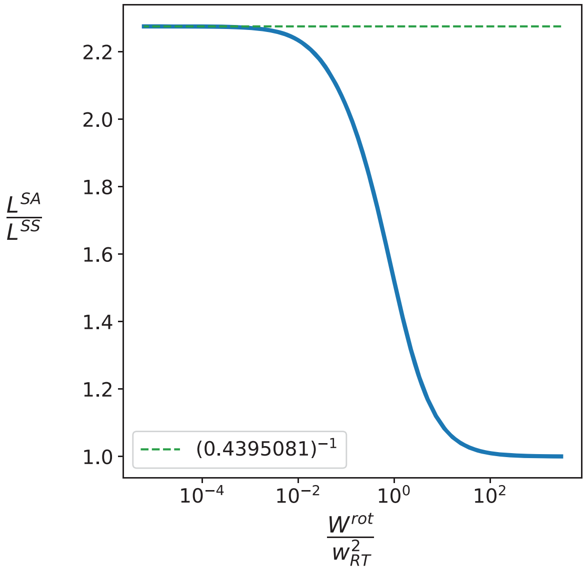

Figure 7. Variation of the drag ratio (indicated by the blue line) in a FCC system under dumbbell-mediated diffusion by the 90° roto-translation mechanism shown in Table 2, along with on-site 90° rotations. All rates are kept the same and only the on-site rotation rate (W^{rot}) is then varied with respect to the roto-translation rate (W^2_{RT}). The inverse of the tracer correlation factor without on-site rotations rates is indicated with the horizontal dotted line. We see that an increasing W^{rot} relative to W^2_{RT} leads to a decrease in the drag ratio. This is because the on-site rotations allow the mixed dumbbells to escape the octahedral cage as shown in Figure 6, leading to increasingly long-ranged mixed dumbbell diffusion.

The PDC ratio is a measure of the relative amount of solute and solvent flux that is observed under a SIA CPG and is thus informative of the segregation behaviour of solutes [48]. If the PDC ratio is high, it indicates higher solute flux than solvent flux towards SIA sinks, thus leading to solute segregation, while a low PDC ratio indicates a lower amount of solute segregation. Since relative pure and mixed dumbbell diffusion fluxes determine the PDC ratio, it can be inferred from their relative formation energies and migration rates.

The results of our PDC calculations on the BCC Fe-S alloys are shown in Figure 8, along with comparisons with the results in [48]. As discussed before, in BCC systems the 60° roto-translation jump is the lowest barrier jump. For Fe-Fe pure dumbbells, the migration barrier for this jump is 0.335

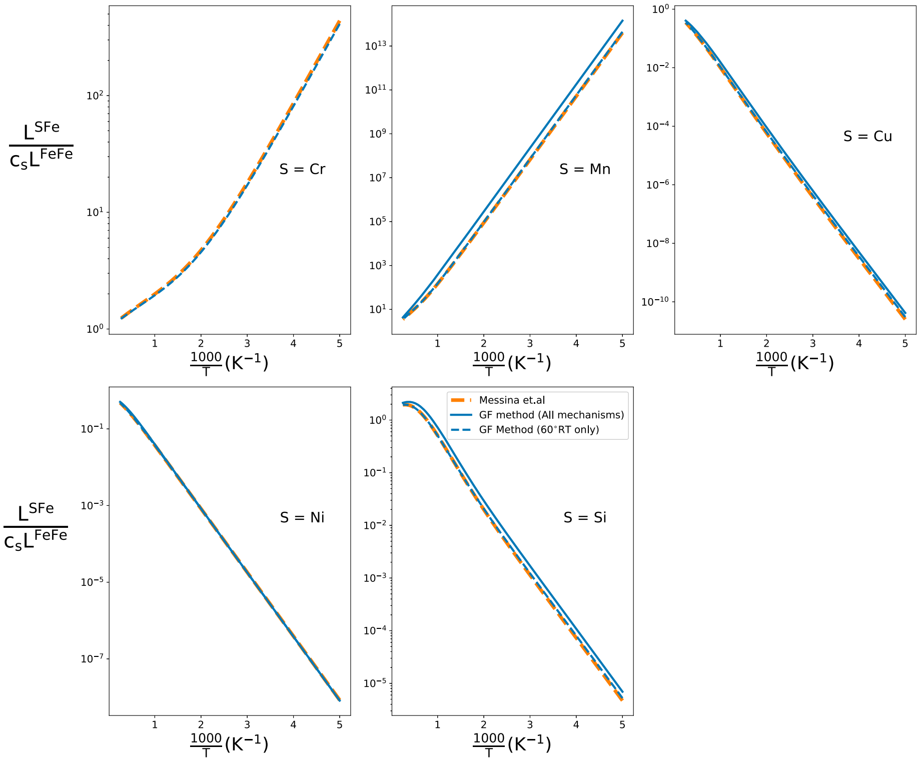

Figure 8. Partial Diffusion Coefficient ratios for solutes in BCC iron for dumbbell-mediated diffusion. Results calculated for the 60° roto-translation mechanism (60°RT) using the Green's function (GF) method are compared with the SCMF results of Messina *et al.* in [47,48] showing good agreement. GF method results with all mechanisms for the respective solutes mentioned in [47] are also shown. For both Cr and Mn, the mixed dumbbells formation barriers are low, while the mixed dumbbell annihilation barriers are high. As a result, the solute transport by the mixed dumbbell diffusion is more effective at lower temperatures, since annihilation is less probable than at high temperatures. For Ni, Cu and Si, the mixed dumbbell is less stable than the most stable nearest neighbour solute-pure dumbbell configuration and hence solute transport by mixed dumbbell diffusion can occur at higher temperatures, where thermal energy can assist in mixed dumbbell formation.

eV. In Fe-Cr and Fe-Mn alloys, the migration barriers for mixed dumbbell roto-translation jumps are lower at 0.241 and 0.316 eV respectively, and also mixed dumbbells are more stable than complex states. As a result, at lower temperatures, mixed dumbbell fluxes are higher than pure dumbbells. Thus, at low temperatures, these solutes can show radiation-induced segregation (as seen in [14] for Fe-Cr alloys). As the temperature increases, thermal energy helps Fe-Fe dumbbells move increasingly as fast as the mixed dumbbells and also brings their formation probabilities closer, thus decreasing the PDC ratio. On the other hand, for the solutes Cu, Ni and Si, mixed dumbbells are less stable than complex states, and the mixed dumbbell roto-translation migration barriers are 0.364, 0.464 and 0.518 eV respectively, leading to more flux of pure dumbbells than mixed dumbbells at lower temperatures and hence the PDC ratio for these solutes are low at lower temperatures and increase with increasing temperature, indicating a higher segregation tendency as temperatures increase. Finally, our obtained results are in agreement with results in [48].

The calculated PDC ratios for the FCC Ni-Cr and Ni-Fe alloys are shown in Figure 9. From Table 1, it can be seen that mixed Fe-Ni interstitial dumbbells are less stable than far separated Fe – Ni/Ni pure dumbbell complex state by 0.11 eV. This high repulsion makes the PDC ratio low at low temperatures, while it increases with increasing temperatures due to increasing thermally assisted mixed dumbbell formation and diffusion. In contrast, Ni-Cr interstitial dumbbells are more stable than a far separated Cr – Ni/

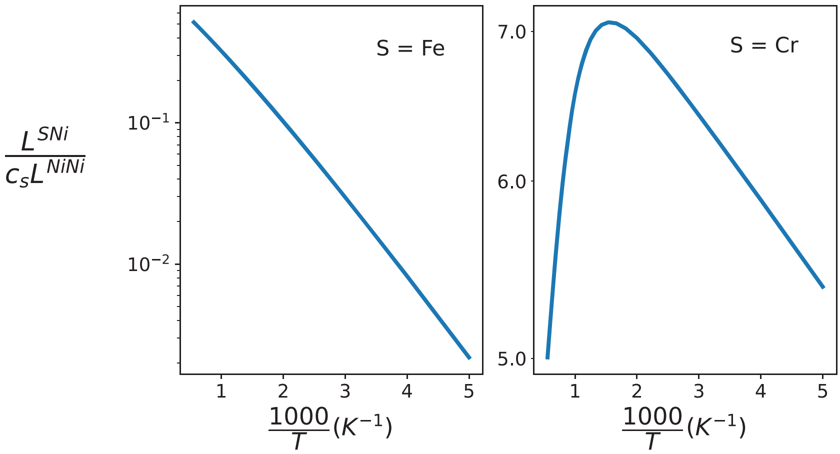

Figure 9. Partial Diffusion Coefficient (PDC) ratios for solutes in FCC Ni for dumbbell-mediated diffusion. For Fe, the PDC ratio increases with increase in temperature, due to some thermally assisted formation and diffusion of mixed dumbbells. Cr almost always exists as mixed dumbbells, and hence the PDC ratio remains within the same order of magnitude, varying relatively weakly compared to Fe. It initially increases with temperature, due to increased diffusion via mixed dumbbell rotations, and shows a decreasing trend at high temperatures due to thermally assisted mixed dumbbell annihilation and pure dumbbell diffusion.

Ni complex state by 0.42 eV. Additionally, as reported in [19], the energy barrier for a mixed dumbbell formation jump from an a-type complex is 0 eV, which implies that as soon as Cr encounters a Ni-Ni dumbbell in a type-a configuration, it almost immediately forms a Ni-Cr mixed dumbbell via an ω^4 jump. Hence the PDC ratio remains consistently higher than Ni-Fe at all temperatures, and varies within the same order of magnitude. As shown in Figure 6, at low temperatures, where on-site rotation rates are very low, mixed dumbbell diffusion is restricted to octahedral cages. The initial increase of the PDC ratio for Cr with temperature can be attributed to the increase in on-site rotation rates which assists long-ranged diffusion of Ni-Cr dumbbells upon escaping the octahedral cage. The subsequent decrease at higher temperatures can be attributed to increased mixed dumbbell annihilation as well as increasing pure dumbbell formation and diffusion probabilities.

4. Summary

The Green's function method in [42] was extended to compute transport coefficients in the dilute limit for solute transport in crystalline solids via dumbbell mediated diffusion with non-truncated correlations. The implemented methodology was validated by computing tracer correlation factors and comparing them to existing data in the literature. Transport coefficient ratios were then computed for several solutes in BCC Fe and FCC Ni based on energetic data available in existing literature. Solute drag ratios in BCC Fe-S alloys exhibit a dual characteristic depending on competing ω^2, ω^3 and ω^4 rates, while in FCC Ni-S alloys, the drag ratios show monotonic behaviour predominantly controlled by on-site rotations of mixed dumbbells. The partial diffusion coefficient ratios were found to depend on the relative stabilities of mixed dumbbells compared to complex states as well as the relative mixed and pure dumbbell migration rates.

Disclosure statement

No potential conflict of interest was reported by the authors.

Funding

This work is sponsored by the NSF program [grant number HDR-1940287].

Code and data availability

The Green's function method for interstitial dumbbell-mediated transport, implemented in Python 3 along with Jupyter notebooks for the dilute FCC

Ni-S (S=Fe, Cr) and BCC Fe-S (S=Cr, Mn, Cu, Ni, Si) alloys and associated data are publicly available at [52].

References

[1] F. Garner.*Radiation damage in austenitic steels*, in *Comprehensive Nuclear Materials*,.Konings R.J.M , ed., Elsevier, Oxford, 2012. pp. 33–95.

[2] T.R. Allen, D. Kaoumi, J.P. Wharry, Z. Jiao, C. Topbasi, A. Kohnert, L. Barnard, A. Certain, K.G. Field, G.S. Was, D.L. Morgan, A.T. Motta, B.D. Wirth, and Y. Yang, *Characterization of microstructure and property evolution in advanced cladding and duct: Materials exposed to high dose and elevated temperature*, J. Mater. Res. 30 (2015), pp. 1246–1274.

[3] J.P. Wharry and G.S. Was, *A systematic study of radiation-induced segregation in ferritic–martensitic alloys*, J. Nuclear Mater. 442 (2013), pp. 7–16.

[4] E.A. Marquis, R. Hu, and T. Rousseau, *A systematic approach for the study of radiation-induced segregation/depletion at grain boundaries in steels*, J. Nuclear Mater. 413 (2011), pp. 1–4.

[5] C. Nellis and C. Hin, *Radiation induced segregation in quaternary fe-ti-y-o alloys*, J. Alloys. Compd. 701 (2017), pp. 82–93.

[6] Z. Jiao and G. Was, *Novel features of radiation-induced segregation and radiation-induced precipitation in austenitic stainless steels*, Acta. Mater. 59 (2011), pp. 1220–1238.

[7] S. Zinkle, P. Maziasz, and R. Stoller, *Dose dependence of the microstructural evolution in neutron-irradiated austenitic stainless steel*, J. Nuclear Mater. 206 (1993), pp. 266–286.

[8] G. Sundell, M. Thuvander, P. Tejland, M. Dahlbäck, L. Hallstadius, and H.-O. Andrén, *Redistribution of alloying elements in zircaloy-2 after in-reactor exposure*, J. Nuclear Materi. 454 (2014), pp. 178–185.

[9] R. Stoller, *Primary radiation damage formation*, in *Comprehensive Nuclear Materials*, Konings R.J.M, ed., Elsevier, Amsterdam, Netherlands, 2012. pp. 293–332.

[10] A.J. Ardell and P. Bellon, *Radiation-induced solute segregation in metallic alloys*, Curr. Opin. Solid State Mater. Sci. 20 (2016), pp. 115–139.

[11] M. Nastar and F. Soisson, *Radiation-induced segregation*, in *Comprehensive Nuclear Materials*, Elsevier, 2012, pp. 471–496.

[12] A.R. Allnatt and A.B. Lidiard, *Some applications of non-equilibrium thermodynamics to solids*, in *Atomic Transport in Solids*, Cambridge University Press, Cambridge, 1993. pp. 181–215.

[13] A.R. Allnatt and A.B. Lidiard, *Atomic movements in solids – phenomenological equations*, in *Atomic Transport in Solids*, Cambridge University Press, Cambridge, 1993. pp. 1–49.

[14] O. Senninger, F. Soisson, E. Martınez, M. Nastar, C.-C. Fu, and Y. Bréchet, *Modeling radiation induced segregation in iron–chromium alloys*, Acta. Mater. 103 (2016), pp. 1–11.

[15] C. Domain and C.S. Becquart, *Ab initio calculations of defects in fe and dilute fe-cu alloys*, Phys. Rev. B. 65 (2001), p. 024103. Available at https://doi.org/10.1103/physrevb.65.024103.

[16] C.-C. Fu, F. Willaime, and P. Ordejón, *Stability and mobility of mono- and di-interstitials in α-fe*, Phys. Rev. Lett. 92 (2004), p. 175503. Available at https://doi.org/10.1103/physrevlett.92.

[17] T.P.C. Klaver, D.J. Hepburn, and G.J. Ackland, *Defect and solute properties in dilute fe-cr-ni austenitic alloys from first principles*, Phys. Rev. B. 85 (2012), p. 174111. Available at https://doi.org/10.1103/physrevb.85.174111.

[18] K.-H. Robrock, *Interstitial diffusion of metallic solutes in irradiated alloys*, Mater. Sci. Forum 15–18 (1987), pp. 537–556.

[19] J. Tucker, R. Najafabadi, T. Allen, and D. Morgan, *Ab initio-based diffusion theory and tracer diffusion in ni–cr and ni–fe alloys*, J. Nuclear Mater. 405 (2010), pp. 216–234.

[20] S. Choudhury, L. Barnard, J. Tucker, T. Allen, B. Wirth, M. Asta, and D. Morgan, *Ab initio based modeling of diffusion in dilute bcc fe–ni and fe–cr alloys and implications for radiation induced segregation*, J. Nuclear Mater. 411 (2011), pp. 1–14.

[21] H. Wiedersich, P. Okamoto, and N. Lam, *A theory of radiation-induced segregation in concentrated alloys*, J. Nuclear Mater. 83 (1979), pp. 98–108.

[22] H. Mehrer, *Correlation in solid-state diffusion*, in *Diffusion in Solids: Fundamentals, Methods, Materials, Diffusion-Controlled Processes*, Springer, Berlin, Heidelberg, 2007. pp. 105–125.

[23] D. Wolf and K. Differt, *Computer simulation of correlated self-diffusion via randomly migrating vacancies in cubic crystals*, Comput. Phys. Commun. 13 (1977), pp. 167.

[24] D. Wolf, *Correlation effects for interstitial-type self-diffusion mechanisms in b.c.c. and f.c.c. crystals*, Philos. Mag. A 47 (1983), pp. 147–167.

[25] A.R. Allnatt, *Einstein and linear response formulae for the phenomenological coefficients for isothermal matter transport in solids*, J. Phys. C: Solid State Phys. 15 (1982), pp. 5605–5613.

[26] A.R. Allnatt and A.B. Lidiard, *Microscopic theories – the master equation*, in *Atomic Transport in Solids*, Cambridge University Press, Cambridge, 1993. pp. 216–246.

[27] M.J. Lloyd, R.G. Abernethy, D.E.J. Armstrong, P.A.J. Bagot, M.P. Moody, E. Martinez, and D. Nguyen-Manh, *Radiation-induced segregation in w-re: From kinetic Monte Carlo simulations to atom probe tomography experiments*, Euro. Phys. J. B 92 (2019), pp. 1–12. Available at https://doi.org/10.1140/epjb/e2019-100244-y.

[28] E. Martınez, O. Senninger, A. Caro, F. Soisson, M. Nastar, and B.P. Uberuaga, *Role of sink density in nonequilibrium chemical redistribution in alloys*, Phys. Rev. Lett. 120 (2018), p. 106101. Available at https://doi.org/10.1103/physrevlett.120.106101.

[29] C. Becquart, A. Barbu, J. Bocquet, M. Caturla, C. Domain, C.-C. Fu, S. Golubov, M. Hou, L. Malerba, C. Ortiz, A. Souidi, and R. Stoller, *Modeling the long-term evolution of the primary damage in ferritic alloys using coarse-grained methods*, J. Nuclear Mater. 406 (2010), pp. 39–54.

[30] F. Soisson, C. Becquart, N. Castin, C. Domain, L. Malerba, and E. Vincent, *Atomistic kinetic monte carlo studies of microchemical evolutions driven by diffusion processes under irradiation*, J. Nuclear Mater. 406 (2010), pp. 55–67.

[31] L.K. Béland, P. Brommer, F. El-Mellouhi, J.-F. Joly, and N. Mousseau, *Kinetic activation-relaxation technique*, Phys. Rev. E. 84 (2011), p. 046704. Available at https://doi.org/10.1103/physreve.

[32] S. Mahmoud, M. Trochet, O.A. Restrepo, and N. Mousseau, *Study of point defects diffusion in nickel using kinetic activation-relaxation technique*, Acta. Mater. 144 (2018), pp. 679–690.

[33] D.K. Chaturvedi and A.R. Allnatt, *Calculation of transport coefficients for matter transport from linear response formulae by a random walk technique with application to the dumb-bell mechanism*, Philos. Mag. A 65 (1992), p. 1169.

[34] J.L. Bocquet, *Solute-and-dumbbell defect diffusion in b.c.c. lattices*, Philos. Mag. A 63 (1991), pp. 157–183.

[35] A. Barbu and A.B. Lidiard, *Solute segregation in dilute bcc alloys under irradiation*, Philos. Mag. A74 (1996), pp. 709–722.

[36] A. Allnatt, A. Barbu, A. Franklin, and A. Lidiard, *Atomic transport in dilute alloys containing interstitial defects*, Acta Metal. 31 (1983), pp. 1307–1313.

[37] M. Nastar, V.Y. Dobretsov, and G. Martin, *Self-consistent formulation of configurational kinetics close to equilibrium: The phenomenological coefficients for diffusion in crystalline solids*, Philos. Mag. A 80 (2000), pp. 155–184.

[38] M. Nastar, *A mean field theory for diffusion in a dilute multi-component alloy: A new model for the effect of solutes on self-diffusion*, Philos. Mag. 85 (2005), pp. 3767–3794.

[39] V. Barbe and M. Nastar, *Phenomenological coefficients in a concentrated alloy for the dumbbell mechanism*, Philos. Mag. 86 (2006), pp. 3503–3535.

[40] V. Barbe and M. Nastar, *Phenomenological coefficients in a dilute BCC alloy for the dumbbell mechanism*, Philos. Mag. 87 (2007), pp. 1649–1669.

[41] T. Schuler, L. Messina, and M. Nastar, *KineCluE: A kinetic cluster expansion code to compute transport coefficients beyond the dilute limit*, Comput. Mater. Sci. 172 (2020), p. 109191.

[42] D.R. Trinkle, *Automatic numerical evaluation of vacancy-mediated transport for arbitrary crystals: Onsager coefficients in the dilute limit using a green function approach*, Philos. Mag. 97 (2017), pp. 2514–2563.

[43] R. Agarwal and D.R. Trinkle, *Uncertainty quantification of solute transport coefficients*, in *Uncertainty Quantification in Multiscale Materials Modeling*, Wang Yan , McDowell David L. , eds., Woodhead Publishing, Sawston, England, 2020. pp. 93–118.

[44] J.A. Yasi and D.R. Trinkle, *Direct calculation of the lattice green function with arbitrary interactions for general crystals*, Phys. Rev. E. 85 (2012), p. 066706. Available at https://doi.org/10.1103/physreve.85.

[45] A.M.Z. Tan and D.R. Trinkle, *Computation of the lattice green function for a dislocation*, Phys. Rev. E. 94 (2016), p. 023308. Available at https://doi.org/10.1103/physreve.94.023308.

[46] D.R. Trinkle, *Variational principle for mass transport*, Phys. Rev. Lett. 121 (2018), p. 235901. Available at https://doi.org/10.1103/physreve.94.023308.

[47] L. Messina, *Dft binding and migration energies, KineCluE transport coefficients, and ris results in ferritic fe-x (x = cr, cu, mn, ni, p, si) dilute alloys* (2019).

[48] L. Messina, T. Schuler, M. Nastar, M.-C. Marinica, and P. Olsson, *Solute diffusion by self-interstitial defects and radiation-induced segregation in ferritic fe–x (x=cr, cu, mn, ni, p, si) dilute alloys*, Acta. Mater. 191 (2020), p. 166.

[49] J. Tucker, *Ab initio-based modeling of radiation effects in the nickel-iron-chromium system*, Ph.D. thesis, School Univ. Wisconsin, 2008.

[50] A.R. Allnatt and A.B. Lidiard, *Random-walk theories of atomic diffusion*, in *Atomic Transport in Solids*, Cambridge University Press, 1993, pp. 337–379.

[51] T. Garnier, M. Nastar, P. Bellon, and D.R. Trinkle, *Solute drag by vacancies in body-centered cubic alloys*, Phys. Rev. B. 88 (2013), p. 134201. Available at https://doi.org/10.1103/physrevb.88.

[52] D. Trinkle and S. Chattopadhyay, *Extension of onsager for dumbbell mediated diffusion*, 2021. Available at https://github.com/sohamch/Onsager.

Appendices

Appendix 1. Translational symmetry

We use translational symmetry to show that we do not need to evaluate every individual element of the Green's function matrix but rather their sums over the solute unit cell location in the initial state; this reduced Green's function can be evaluated as the pseudo-inverse of a similarly reduced transition rate matrix. We denote with χ generic states (complex or mixed) without considering the solute unit cell location. This means that for a complex state $\mathbf{R}_s\mathbf{u}_s\mathbf{R}_d\mathbf{u}_d\mathbf{o}_d$, χ represents the part $\mathbf{u}_s\mathbf{R}_d\mathbf{u}_d\mathbf{o}_d$, so that $\mathbf{R}_s\chi \equiv \mathbf{R}_s\mathbf{u}_s\mathbf{R}_d\mathbf{u}_d\mathbf{o}_d$. Recall that in a complex state, the vector $\mathbf{R}_d$ gives the dumbbell unit cell location relative to the solute's. Similarly for a mixed state $\mathbf{R}_m\mathbf{u}_m\mathbf{o}_m$, χ would represent the part $\mathbf{u}_m\mathbf{o}_m$, so that $\mathbf{R}_m\chi \equiv \mathbf{R}_m\mathbf{u}_m\mathbf{o}_m$ (recall that the solute is a part of the mixed dumbbell and is present at the same location $\mathbf{R}_m + \mathbf{u}_m$). A sum of the form $\sum_{\mathbf{R}_s\chi}$ then represents a sum over all states, both complex and mixed, *i.e.*, we track the solute unit cell separately. The transport coefficients can then be evaluated as,

$$\begin{aligned} V_0 k_B T L^{\alpha\beta} = &\frac{1}{2}\sum_{\mathbf{R}_s\chi}\sum_{\mathbf{R}'_s\chi'} p^0_{\mathbf{R}_s\chi} W_{\mathbf{R}_s\chi,\mathbf{R}'_s\chi'}\,\delta\mathbf{x}^{\alpha}(\mathbf{R}_s\chi \to \mathbf{R}'_s\chi') \otimes \delta\mathbf{x}^{\beta}(\mathbf{R}_s\chi \to \mathbf{R}'_s\chi') \\ &+ \sum_{\mathbf{R}_s\chi}\sum_{\mathbf{R}'_s\chi'} p^0_{\mathbf{R}_s\chi}\mathbf{v}^{\alpha}_{\mathbf{R}_s\chi} \otimes G_{\mathbf{R}_s\chi,\mathbf{R}'_s\chi'}\mathbf{v}^{\beta}_{\mathbf{R}'_s\chi'} \end{aligned} \tag{A1}$$

Since the probabilities, velocities, displacements, Green's function and rates all obey translational invariance, we can write

$$\begin{aligned} \frac{V_0}{N} k_B T L^{\alpha\beta} = &\frac{1}{2}\sum_{\chi}\sum_{\mathbf{R}'_s\chi'} p^0_{\mathbf{0}\chi} W_{\mathbf{0}\chi,\mathbf{R}'_s\chi'}\,\delta\mathbf{x}^{\alpha}(\mathbf{0}\chi \to \mathbf{R}'_s\chi') \otimes \delta\mathbf{x}^{\beta}(\mathbf{0}\chi \to \mathbf{R}'_s\chi') \\ &+ \sum_{\chi}\sum_{\chi'} p^0_{\mathbf{0}\chi}\mathbf{v}^{\alpha}_{\mathbf{0}\chi} \otimes \left(\sum_{\mathbf{R}'_s} G_{\mathbf{0}\chi,\mathbf{R}'_s\chi'}\right)\mathbf{v}^{\beta}_{\mathbf{0}\chi'} \end{aligned} \tag{A2}$$

where N is the number of unit cells in our solid. We then define the reduced Green's function matrix as $\overline{\mathbf{G}}$ so that $\overline{G}_{\chi\chi'} = \sum_{\mathbf{R}'_s} G_{\mathbf{0}\chi,\mathbf{R}'_s\chi'}$, which has the blocked structure of the form shown in Equation (28) depending on when χ and χ' represent complex or mixed dumbbell states.

We next outline the derivation of the inverse relationship between the reduced Green's function and transition rate matrices, *i.e.*, Equation (29). We first express the transition rates between states as the representation of a transition rate operator $\widehat{W}$ in the state space spanned by state basis vectors $|\mathbf{R}_s\chi\rangle$ as

$$W_{\mathbf{R}_s\chi,\mathbf{R}'_s\chi'} = \left\langle \mathbf{R}_s\chi|\widehat{W}|\mathbf{R}'_s\chi'\right\rangle \tag{A3}$$

We then define a unitary translation operator $\hat{T}_{\mathbf{a}}$ that translates the solute unit cell position by a vector $\mathbf{a}$ so that for any state vector $|\mathbf{R}_s\chi\rangle$

$$\widehat{T}_{\mathbf{a}}|\mathbf{R}_s\chi\rangle = |(\mathbf{R}_s + \mathbf{a})\chi\rangle \tag{A4}$$

Due to translational invariance in terms of solute unit cell location, the transition rate operator will commute with the lattice translation operator since

$$W_{(\mathbf{R}_s+\mathbf{a})\chi,(\mathbf{R}'_s+\mathbf{a})\chi'} = \left\langle (\mathbf{R}_s + \mathbf{a})\chi|\widehat{W}|(\mathbf{R}'_s + \mathbf{a})\chi'\right\rangle = \left\langle \mathbf{R}_s\chi|\widehat{T}^{\dagger}_{\mathbf{a}}\widehat{W}\widehat{T}_{\mathbf{a}}|\mathbf{R}'_s\chi'\right\rangle \tag{A5}$$

and from Equations (A3) and (A5), due to the invariance of the transition rates under the same lattice translation of the states,

$$\widehat{T}_{\mathbf{a}}^{\dagger}\widehat{W}\widehat{T}_{\mathbf{a}} = \widehat{W} \tag{A6}$$

or

$$\widehat{W}\widehat{T}_{\mathbf{a}} = \widehat{T}_{\mathbf{a}}\widehat{W} \tag{A7}$$

Due to this commutation relationship, the representation of the transition rate operator in the basis of the eigenfunctions of $\widehat{T}_{\mathbf{a}}$ can be made block-diagonal. We first note that we can choose eigenfunctions $\phi_{\mathbf{q}_s,\chi}$ of $T_{\mathbf{a}}$ to be indexed by reciprocal lattice vectors $\mathbf{q}_s$ and states χ, so that in the state space they can be represented as $\phi_{\mathbf{q}_s,\chi} = \frac{1}{\sqrt{N}}\sum_{\mathbf{R}'_s\chi'} e^{-i\mathbf{q}_s\cdot\mathbf{R}'_s}\delta_{\chi\chi'}|\mathbf{R}'_s\chi'\rangle$ (here δ denotes the Kronecker delta) with the corresponding eigenvalue being $e^{i\mathbf{q}_s\cdot\mathbf{a}}$ for all $\phi_{\mathbf{q}_s,\chi}$ with the same $\mathbf{q}_s$. These eigenfunctions are orthonormal, i.e. $\langle\phi_{\mathbf{q}_s,\chi}|\phi_{\mathbf{q}'_s,\chi'}\rangle = \delta_{\chi,\chi'}\delta(\mathbf{q}_s - \mathbf{q}'_s)$ for $\mathbf{q}_s$ and $\mathbf{q}'_s$ in the first Brillouin zone and they block-diagonalise the transition rate operator with respect to $\mathbf{q}_s$ since

$$\begin{aligned}
W_{\chi\chi'}(\mathbf{q}_s, \mathbf{q}'_s) &= \left\langle\phi_{\mathbf{q}_s,\chi}|\widehat{W}|\phi_{\mathbf{q}'_s,\chi'}\right\rangle \\
&= \frac{1}{N}\sum_{R_s\chi''}\sum_{R'_s\chi'''} e^{i\mathbf{q}_s\cdot\mathbf{R}_s}\delta_{\chi\chi''}W_{\mathbf{R}_s\chi'',\mathbf{R}'_s\chi'''}e^{-i\mathbf{q}'_s\cdot\mathbf{R}'_s}\delta_{\chi'\chi'''} \\
&= \frac{1}{N}\sum_{R_s,R'_s} e^{i\mathbf{q}_s\cdot\mathbf{R}_s}W_{\mathbf{R}_s\chi,\mathbf{R}'_s\chi'}e^{-i\mathbf{q}'_s\cdot\mathbf{R}'_s} \\
&= \frac{1}{N}\sum_{R_s} e^{i(\mathbf{q}_s-\mathbf{q}'_s).\mathbf{R}_s}\sum_{R'_s}W_{\mathbf{R}_s\chi,\mathbf{R}'_s\chi'}e^{-i\mathbf{q}'_s\cdot(\mathbf{R}'_s-\mathbf{R}_s)} \\
&= \delta(\mathbf{q}_s - \mathbf{q}'_s)\sum_{R'_s}W_{\mathbf{0}\chi,\mathbf{R}'_s\chi'}e^{i\mathbf{q}_s\cdot\mathbf{R}'_s}
\end{aligned} \tag{A8}$$

The Green's function $\mathbf{G}$, the inverse of the transition rate, will then also share the same block diagonal structure, and for every $\mathbf{q}_s$, their blocks will be inverses of each other, i.e.

$$[\mathbf{G}(\mathbf{q}_s)]_{\chi\chi'} = [\mathbf{W}(\mathbf{q}_s)]^{-1}_{\chi\chi'} \tag{A9}$$

where $W_{\chi\chi'}(\mathbf{q}_s) = \sum_{R'_s}W_{\mathbf{0}\chi,\mathbf{R}'_s\chi'}e^{i\mathbf{q}_s\cdot\mathbf{R}'_s}$ and $G_{\chi\chi'}(\mathbf{q}_s) = \sum_{R'_s}G_{\mathbf{0}\chi,\mathbf{R}'_s\chi'}e^{i\mathbf{q}_s\cdot\mathbf{R}'_s}$. At $\mathbf{q}_s = \mathbf{0}$, $\mathbf{W}(\mathbf{q}_s)$ and $\mathbf{G}(\mathbf{q}_s)$ become the matrices $\overline{\mathbf{W}}$ and $\overline{\mathbf{G}}$ in Equations (30) and (28) respectively.

Appendix 2. Non-ergodicity in low-dimensional jump networks

In the FCC 90° roto-translation mechanism shown in Table 2, we can see that once we fix the initial site, the initial orientation and the final site of a pure dumbbell after a jump, the final pure dumbbell orientation is uniquely determined. This leads to a non-ergodic diffusion process for the pure dumbbells, with disconnected jump networks depending on the initial starting state. A simplified example of this is shown in Figure A1, where we have 90-degree roto-translation of dumbbells on a 1D chain of sites. As can be seen in the figure, there are two types of distinct jump networks that can arise depending on how we fix the starting dumbbell orientation, with no dumbbell jump connecting the two networks, leading to non-ergodicity. In Appendix 3, we show the implications of non-ergodicity for this example jump network in Fourier space. Although geometrically more complex, the FCC roto-translation mechanism for pure dumbbells is conceptually similar to this 1D jump mechanism, and depending on the chosen starting $\langle 100\rangle$-type dumbbell orientation at a certain starting site, we'll have three disconnected jump networks in the solid, leading to the matrix $\mathbf{W}$ in Equation (3) being block diagonal with three diagonal blocks, representing each such jump network. Such non-ergodicity reduces the symmetry of the system, and we get singular matrices $\widetilde{\boldsymbol{\Omega}}(\mathbf{q})$ for other reciprocal lattice vectors $\mathbf{q}$ at the first Brillouin Zone edges as well, instead of just at $\mathbf{q} = \mathbf{0}$ (see Appendix 3). In our calculations, the Moore-Penrose pseudo-inverse of $\widetilde{\boldsymbol{\Omega}}(\mathbf{q})$ instead of the inverse is computed and used in the semi-continuum approach to inverse transform $\widetilde{\mathbf{g}}(\mathbf{q})$.

For the BCC rigid translation mechanism, pure dumbbells can only maintain a single $\langle 110\rangle$ orientation throughout the diffusion process, and their diffusion is always restricted to the corresponding $\{1\bar{1}0\}$ plane which contain the orientation vector. This again leads to disconnected jump networks depending on the initial starting orientation, and all the eigenvalues of $\widetilde{\boldsymbol{\Omega}}(\mathbf{q})$ will be zero at $\mathbf{q} = \mathbf{0}$, as shown in Appendix 3 for a simplified case of a 1D lattice. This leads to the $\mathbf{D}(\mathbf{q}) = \mathbf{DD}(\mathbf{q})$ block becoming a 6×6 matrix as all other blocks are zero. Hence, the block inversion procedure Equation (53) onward cannot be applied, since Equation (54) is valid for a $1 \times 1 \mathbf{DD}(\mathbf{q})$ block. However, for this particular mechanism, we note that dumbbell diffusion is two dimensional. Further, since diffusion characteristics of dumbbells restricted to $\{1\bar{1}0\}$ planes will be the same by symmetry, we can study this diffusion mechanism for a single $\{1\bar{1}0\}$ plane.

To simulate rigid dumbbell diffusion on a BCC $\{1\bar{1}0\}$ plane, we set up a two-dimensional face-centered rectangular lattice with lattice vectors $[0, a_0]$ and $[a_0\sqrt{2}, 0]$, and allow two-dimensional dumbbells with orientation vectors along $[1, 0]$ for pure dumbbells, and $[1, 0]$ and $[-1, 0]$ for mixed dumbbells. Note that under the two-fold symmetry of this lattice, there will be no other allowed dumbbell orientations at a site. We then allow both pure and mixed dumbbell jumps to occur via rigid translation from the corner to face centre of this 2D lattice, equivalent to the rigid translation jump mechanism shown in Table 2. The tracer correlation factor for this two-dimensional diffusion mechanism is then computed as the ratio of the trace of $L^{A^*A^*}$ to the trace of L^{A^*A}. This is the value reported in Table 2 for the rigid translation mechanism.

We note from our results on the BCC and FCC alloys however, that these diffusion mechanisms are almost always accompanied by either on-site rotations or by other lower

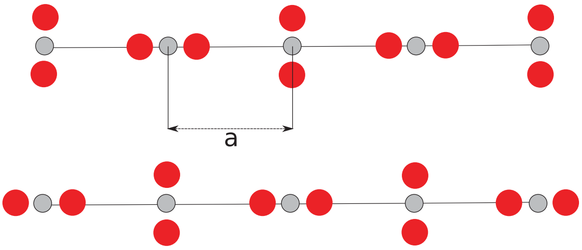

Figure A1. Non-ergodic jump networks involving only two types of dumbbell orientations (atoms shown as red circles), horizontal and vertical, on a 1D chain of sites (shown as grey circles) with lattice parameter *a*. A jump by a dumbbell to a neighboring site is always accompanied by a change of orientation by 90 degrees. The jump network at the top has the opposite sequence of dumbbell orientations on the sites as the jump network at the bottom. There is no 90-degree roto-translation jump that can connect these two jump networks.

energy diffusion mechanisms (such as the 60° roto-translation mechansim in BCC crystals). In either case, dumbbell mediated diffusion becomes ergodic and hence these issues don't arise.

Appendix 3. Singularities for non-ergodic diffusion mechanisms

We derive the Fourier transform of the symmetrised rate matrix $\widetilde{\mathbf{\Omega}}(q)$ for the dumbbell transitions on a 1d chain of sites shown in Figure A1 involving 90° nearest neighbour roto-translation jumps of horizontal (h) and vertical (v) oriented dumbbells. This simplified example is designed to show how additional singularities can arise at Brillouin Zone edges for a non-ergodic diffusion mechanism. The Fourier transform of the symmetrised rate matrix (without rotating the basis using its eigenvectors at $\mathbf{q}=\mathbf{0}$) is given by

$$\widetilde{\Omega}_{ab}(q)=\sum_{x}\Omega^{0}_{0a,xb}\ e^{-iqx} \tag{A10}$$

where $\Omega^{0}_{0a,xb}$ is the symmetrised tansition rate matrix element that corresponds to a dumbbell with initial orientation a at the origin site, jumping to form a dumbbell with orientation b at the site located at distance x from it. For this two-state system where a, $b\in\{h, v\}$, the matrix $\widetilde{\mathbf{\Omega}}(q)$ will be 2×2 and of the the form

$$\widetilde{\Omega}(q)=\begin{bmatrix}\widetilde{\Omega}_{hh}(q) & \widetilde{\Omega}_{hv}(q)\\ \widetilde{\Omega}_{vh}(q) & \widetilde{\Omega}_{vv}(q)\end{bmatrix}=\begin{bmatrix}-2W^{0} & 2W^{0}\cos(qa)\\ 2W^{0}\cos(qa) & -2W^{0}\end{bmatrix} \tag{A11}$$

where W^0 is the 90° roto-translation rate.

The variation of the eigenvalues of the Fourier transform matrix in Equation (A11) within the first Brillouin zone is shown in Figure A2. It can be seen that the non-ergodicity in the jump mechanism manifests itself as additional singularities at the edges of the first Brillouin zone. However, such singularities are removed upon introducing on-site $h\leftrightarrow v$ rotations with a rate W_r. This leads to $-W_r$ being added to the diagonal elements of Equation (A11), and $+W_r$ being added to the off-diagonal elements. As can be seen from Figure A2, this removes the zero eigenvalues at the edges of the Brillouin zone, and thus we only have a singularity at the Brillouin zone origin.

Appendix 4. Numerical error analysis and computational complexity

We analyse numerical errors in the $g^{0,d}$ Green's function values similarly to the case of vacancies in [42], and provide computational time analysis for transport coefficients. For this purpose, we choose to simulate tracer diffusion via $\langle 110\rangle$ in a BCC system with the 60° roto-translation mechanism, with a first nearest neighbour thermodynamic shell (although all interaction energies are set to zero) and all rates are fixed to 1. For the analytical part of the inverse transformation process of $\widetilde{\mathbf{g}}(\mathbf{p})$ as mentioned in Section 2.7, the same threshold parameters were used as for the case of vacancies (see Section 2.1 and 4.1 in [42] for details) as they were found to provide sufficiently accurate inverse transforms up to 10 decimal places. Any error in $g^{0,d}$ values mainly arises from the numerical integration of the semi-continuum piece.

To analyse the effect of numerical quadrature for our inverse Fourier transform, we compute pure dumbbell Green's function elements $g^{0,d}_{\mathbf{R}_\mathrm{d}\mathbf{u}_\mathrm{d}\mathbf{o}_\mathrm{d},\mathbf{R}'_\mathrm{d}\mathbf{u}'_\mathrm{d}\mathbf{o}'_\mathrm{d}}$, setting both $\mathbf{o}_\mathrm{d}$, and $\mathbf{o}'_\mathrm{d}$ to xy-oriented dumbbells, and see how their errors behave as a function of the number of $\mathbf{k}$-points. We note that the BCC lattice being monoatomic, $\mathbf{u}_\mathrm{d}=\mathbf{u}'_\mathrm{d}=0$. With $\mathbf{R}_\mathrm{d}=0$ we

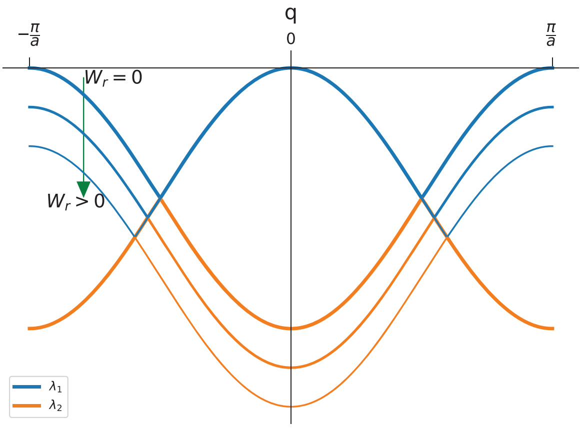

Figure A2. Variation of the two eigenvalues (λ_1 and λ_2) of the Fourier transform of the symmetrised rate matrix in the first Brillouin zone for the non-ergodic 1D 90° re-orienting nearest-neighbour dumbbell jump mechanism shown in Figure A1, with varying on-site 90° rotation rates (W_r). As shown with the green arrow, without on-site rotations being allowed ($W_r = 0$), one of the two eigenvalues becomes zero at the origin and at the left and right edges of the Brilouin zone. On introducing on-site rotations of the dumbbells with non-zero rotation rates, the jump network becomes ergodic and the singularities at the Brillouin zone edges are removed.

evaluate the Green's function for when $\mathbf{R}'_\mathrm{d} = 0$ (we call this $g(\mathbf{0})$ henceforth) and for when $\mathbf{R}'_\mathrm{d} = 2\hat{\mathbf{i}} + 2\hat{\mathbf{j}} + 2\hat{\mathbf{k}}$ (we call this $g(\mathbf{R})$ henceforth). The second case corresponds to the Green's function element between two pure dumbbells with xy-orientations dumbbells that are separated by the maximum possible distance in the kinetic shell. We also look at the nature of their difference since it is the difference between Green's function elements that contributes to the transport coefficients.

In order to compute the errors arising out of numerical errors, we compute $g(\mathbf{0})$, $g(\mathbf{R})$ and $|g(\mathbf{0}) - g(\mathbf{R})|$ for increasing number of $\mathbf{k}$-points (N_{kpt}) in the Brillouin zone. We then extrapolate the obtained values to estimate the values at infinite $\mathbf{k}$-points and then subtract this from the obtained values to get the estimated numerical integration error. Table A1

Table A1. Green's function values as a function of the number of **k**-points (N_{kpt}) and the number of symmetrically reduced k-points(N_{red}). All values are computed for xy-oriented $\langle 110 \rangle$ dumbbells in a BCC system with unit lattice parameter and for the 60° roto-translation mechanism, and $\mathbf{R} = 2\hat{\mathbf{i}} + 2\hat{\mathbf{j}} + 2\hat{\mathbf{k}}$.

Grid	N_{kpt} (N_{red})	$g(\mathbf{0})$	$g(\mathbf{R})$	$g(\mathbf{0}) - g(\mathbf{R})$
6 × 6 × 6	216 (16)	−0.151 412 013 464	−0.008 388 832 684	-0.143 023 180 780
10 × 10 × 10	1000 (48)	−0.151 262 509 102	−0.002 422 301 213	−0.148 840 207 890
14 × 14 × 14	2744 (109)	−0.151 257 955 867	−0.002 386 185 418	−0.148 871 770 449
18 × 18 × 18	5832 (210)	−0.151 257 350 380	−0.002 385 037 675	−0.148 872 312 705
22 × 22 × 22	10648 (363)	−0.151 257 202 450	−0.002 384 852 600	−0.148 872 349 849
26 × 26 × 26	17576 (580)	−0.151 257 154 493	−0.002 384 798 793	−0.148 872 355 700
30 × 30 × 30	27000 (860)	−0.151 257 135 826	−0.002 384 778 779	−0.148 872 357 048
34 × 34 × 34	39304 (1228)	−0.151 257 127 554	−0.002 384 770 105	−0.148 872 357 449
38 × 38 × 38	54872 (1689)	−0.151 257 123 506	−0.002 384 765 917	−0.148 872 357 589
42 × 42 × 42	74088 (2254)	−0.151 257 121 370	−0.002 384 763 723	−0.148 872 357 647
46 × 46 × 46	97336 (2934)	−0.151 257 120 170	−0.002 384 762 496	-0.148 872⍰⍰357 674
50 × 50 × 50	125000 (3742)	−0.151 257 119 463	−0.002 384 761 774	−0.148 872 357 689

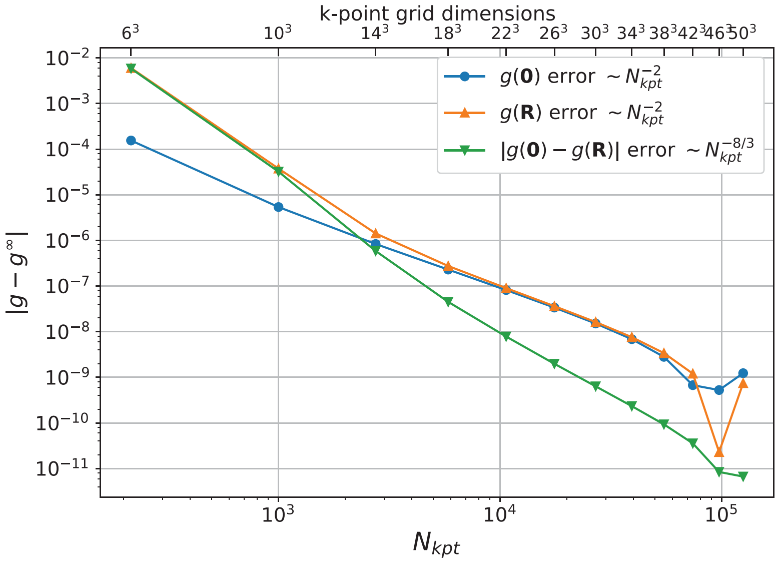

Figure A3. Scaling of the estimated integration errors in Green's function values of $g(\mathbf{0})$, $g(\mathbf{R})$ and $|g(\mathbf{0}) - g(\mathbf{R})|$ compared to an extrapolated infinite k-point density value (g^∞) for each as a function of the number of **k**-points in the first Brillouin zone. A Nearly power-law decay is seen in the errors up to around 10^5**k**-points, beyond which numerical integration errors start to get dominated by round-off errors.

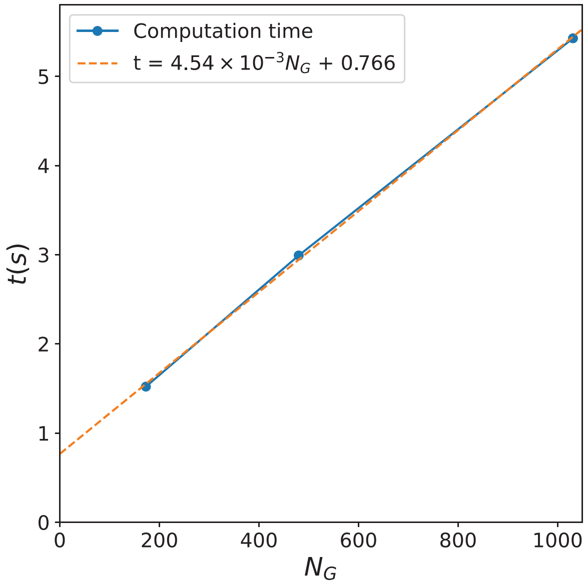

Figure A4. Scaling of the calculation time (t) in seconds for a single transport coefficients calculation, as a function of the number of symmetry-unique values of $g^{0,d}$ to be computed (N_G) for the 60° roto-translation jumps of ⟨110⟩ dumbbells in a BCC system. All times are reported as averages over 50 computations with 18^3**k**-points in the first Brillouin zone. Linear scaling of the time is observed with respect to N_G and typically only a few seconds are required to get the transport coefficients.

shows the values of the Green's function elements with increasing **k**-points, and their deviation from extrapolated infinite **k**-points density value are shown in Figure A3.

We find that up to $\sim 10^5$ **k**-points, integration errors play a dominant role and the errors show power-law decay as a function of the number of **k**-points, which illustrates the controllable behaviour of the errors. We find that $g(\mathbf{0})$ and $g(\mathbf{R})$ errors decay approximately as $\sim N_{kpt}^{-2}$, while $|g(\mathbf{0}) - g(\mathbf{R})|$ errors decay approximately as $\sim N_{kpt}^{-8/3}$. Around $\sim 10^5$ k-points, numerical round off errors start to dominate over the integration errors and fluctuations are seen to occur in the error trend. In our work, we used 18^3 grid size keep computation time reasonably small as well as get small numerical errors of $\sim 10^{-8}$ in the Green's function differences. A similar controllable behaviour of the numerical integration errors was also reported for vacancies in [42].

Next, in Figure A4 we show the computation time for the transport coefficient in the same system as a function of the number of unique bare dumbbell Green's function ($g^{0,d}$) computations needed to be performed within the kinetic shell, N_G which gives a measure of the 'size' of the problem. Each computation time was obtained by averaging over 50 computations after all the states and state-vector orbit data were generated. We find that it takes a few seconds to complete a calculation for even large kinetic shells with $N_G > 1000$ and that the time scales almost linearly with N_G.